Systematic studies of the H.E.S.S. camera calibration

Diplomarbeit
von
Arnim Balzer

Erlangen Centre for Astroparticle Physics
Physikalisches Institut 2
Lehrstuhl für Physik
Friedrich-Alexander-Universität
Erlangen-Nürnberg

1. Gutachter: Prof. Ch. Stegmann
2. Gutachter: Prof. G. Anton

31. Mai 2010

Abstract

The High Energy Stereoscopic System (H.E.S.S.) is an array of four imaging atmospheric Cherenkov telescopes, situated in the Khomas Highland in Namibia. Since the inauguration in 2004, it has discovered numerous new sources of very high energy (VHE, $>100\,\mathrm{GeV}$) gamma-rays. One highlight is the recent detection of very faint gamma radiation from the star burst galaxy NGC 253, the radio galaxy Centaurus A and the supernova remnant SN 1006 [1–3]. All three detections are based on more than 100 h of observation time accumulated over several years. This is necessary, because the sources have fluxes in the order of $\approx 1\,\%$ of the Crab Nebula. An absolute necessity of those long term observation campaigns is a detailed understanding of the camera calibration and systematics, which will be investigated in detail in the course of this thesis: The position and length of the read out window of the photomultipliers and its dependencies of the shower parameters will be examined, as well as the long term stability of the camera calibration. Furthermore, known hardware problems are discussed. However, the main focus of this thesis is on the correct estimation of the baselines of the photomultipliers. The two methods currently in use, as well as an improved method, and their comparison will be presented. At last, the online analysis, a real time analysis running in parallel with the data taking of the telescope system, and the standard analyses will be compared. For instance, the difference in the calibration and the influence on the significance of the detection and the spectrum of sources will be shown.

Kurzfassung

Das High Energy Stereoscopic System (H.E.S.S.) besteht aus vier abbildenden atmosphärischen Cherenkov-Teleskopen im Khomas Hochland in Namibia. Seit der Einweihung in 2004 wurden zahlreiche neue Quellen sehr hochenergetischer Gammastrahlen entdeckt ($>100\,\mathrm{GeV}$). Insbesondere die vor kurzem erfolgte Detektion von sehr schwacher Gammastrahlung aus der Richtung der Starburstgalaxie NGC 253, der Radiogalaxie Centaurus A und des Supernovaüberrests SN 1006. Alle drei Detektionen erforderten Belichtungszeiten von über 100 Stunden, akkumuliert über einem Zeitraum von mehreren Jahren. Dies is notwendig, da die Quellen Flüsse in der Ordnung von $\approx 1\,\%$ des Krebs Nebels haben. Eine absolute Notwendigkeit dieser Langzeitobservationskampagnen ist ein detailliertes Verständniss der Kamerakalibration und -systematik, welche im Rahmen dieser Diplomarbeit im Detail vorgestellt wird: Sowohl die Position und die Länge des Auslesefensters der Photomultiplier und deren mögliche Abhängigkeiten von den Schauerparametern, als auch die Langzeitstabilität der Kamerakalibration werden überprüft. Zusätzlich werden bekannte Hardwareprobleme diskutiert. Der Schwerpunkt dieser Diplomarbeit ist jedoch die korrekte Bestimmung der Nulllinien der Photomultiplier. Sowohl die zwei Methoden, welche im Moment benutzt werden, als auch eine verbesserte Methode und ein Vergleich dieser werden vorgestellt. Zum Schluss werden die Onlineanalyse, eine Echtzeitanalyse welche parallel zur Datennahme des Teleskopsystems läuft, und die Standardanalysen verglichen. Dabei werden die Unterschiede in der Kalibration und der Einfluss auf die Signifikanz der Detektion und auf das Spektrum von Quellen gezeigt.

Contents

1 Introduction **1**

2 Detection of very high energy gamma-rays **2**
2.1 Air shower formation . . . 2
2.2 Cherenkov radiation . . . 3
2.3 Imaging atmospheric Cherenkov technique . . . 5
2.4 Hillas parametrization of air showers . . . 6
2.5 Primary particle identification . . . 8

3 The H.E.S.S. experiment **9**
3.1 Telescope dishes and mirrors . . . 10
3.2 Camera layout . . . 10

4 Camera calibration **13**
4.1 Readout window of the analog ring sampler . . . 13
4.1.1 Pixel amplitude dependencies . . . 15
4.1.2 Shower energy dependencies . . . 16
4.1.3 Pixel position dependencies . . . 16
4.1.4 Shower distance dependencies . . . 17
4.2 Calibration procedure . . . 18
4.2.1 Converting ADC values to photo electron intensities . . . 18
4.2.2 Calibration devices . . . 19
4.2.3 Pedestal estimation . . . 20
4.2.4 ADC to photo electron coefficient . . . 20
4.2.5 HighGain to LowGain ratio . . . 21
4.2.6 Flatfielding . . . 22
4.3 Examples of unusable pixels . . . 23
4.4 Evolution of calibration coefficients over time . . . 24

5 Systematic studies of pedestal estimation methods **27**
5.1 Pedestal estimation methods used in the DST production . . . 27
5.1.1 Average pedestal estimation . . . 28
5.1.2 Average pedestal estimation with a time gradient . . . 28
5.1.3 Comparison of Hillas parameter distributions . . . 29
5.2 Improved pedestal estimation method . . . 30
5.2.1 Determination of the improved pedestal estimation method's parameters 31
5.2.2 Correction of baseline oscillations . . . 35
5.2.3 Improvement over other methods . . . 37
5.2.4 Influence on the Hillas parameters . . . 38
5.2.5 Influence on the significance . . . 39
5.2.6 Influence on the spectrum . . . 40

6 H.E.S.S. online analysis **42**
6.1 Integration into the DAQ 42
6.2 Differences from a standard Hillas analysis 43
6.3 Comparisons of the online and the offline analyses 45
6.3.1 Pedestal distributions 45
6.3.2 Hillas distributions 45
6.3.3 Point sources 47
6.3.4 Extended sources 51

7 Conclusion and Outlook **55**

1 Introduction

The first detected source of very high energy (VHE, corresponding to particle energies between 100 GeV up to $\mathcal{O}(100\,\mathrm{TeV})$) gamma-rays was the Crab Nebula. This was achieved using the Whipple telescope in the 1980's [4], thus establishing the imaging atmospheric Cherenkov technique (IACT). Since the last twenty years the number of known sources increased to over one hundred [5]. A major part in this development played the High Energy Stereoscopic System (H.E.S.S.). With its, compared to other Cherenkov telescopes, superior field of view of 5° and its location in the Southern Hemisphere, the first scan of the galactic plane in the VHE gamma-ray regime was conducted [6, 7]. This scan alone resulted in the discovery of more than 50 previously unknown sources. The capabilities of the H.E.S.S. instrument were further demonstrated by the recent detection of several very faint VHE gamma-ray sources. This includes the star burst galaxy NGC 253 as a new source class, with an integrated flux of gamma-rays above 220 GeV of $(5.5 \pm 1.0_{\mathrm{stat}} \pm 2.8_{\mathrm{sys}}) \cdot 10^{-13}\,\mathrm{cm}^{-2}\,\mathrm{s}^{-1}$ corresponding to 0.3 % of the flux of the Crab Nebula [1]. The significance of the detection was $5.2\,\sigma$ with a live time of 119 h. An excess sky map of NGC 253 is shown in Figure 1.1 (left) together with the other two faint sources Centaurus A (middle) and SN 1006 (right). All three sources have been observed for over 100 h, over the course of several years, and have fluxes in the order of ≈ 1 % of the Crab Nebula [2, 3]. Together with the low statistical significances around $\approx 5\,\sigma$, it is clear that the calibration of the instrument is of the utmost importance.

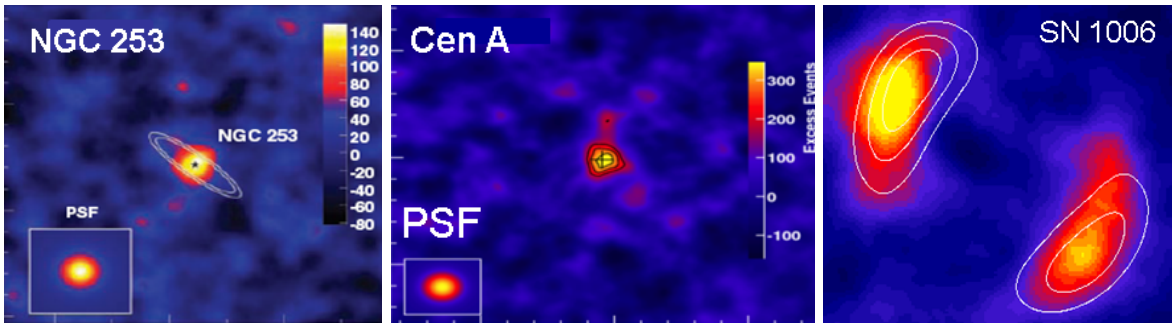

Figure 1.1: *Shown from left to right are the excess sky maps of NGC* 253*, Centaurus A and SN* 1006 *[1–3]. A similarity of theses sources are the long observation times in the order of* 100 *h, as well as fluxes as low as* $\mathcal{O}(1\,\%)$ *of the flux of the Crab Nebula.*

This thesis begins with an introduction into the detection of cosmic gamma radiation. Furthermore, the H.E.S.S. experiment will be presented, with a focus on the layout of the cameras and its electronics. Adjacent, an in depth look at the calibration of the cameras will be given, including detailed studies of the baseline estimation of the photomultipliers of the cameras. At last, the difference of the online analysis, an real time analysis running in parallel with the data taking of the telescope system, and the standard analyses will be presented.

2 Detection of very high energy gamma-rays

With the discovery of the cosmic radiation by Victor Hess in 1912, the door to a new and fascinating branch of physics was opened. At first, the cosmic radiation was mainly used to search for new particles, because at that time no proper particle accelerators were available. With the introduction of high luminosity accelerators, the focus of research was shifted to the study of the origin and propagation of the cosmic radiation. Today, the general characteristics of the cosmic radiation are well know. For example, the typical composition of the cosmic radiation, hitting the earth's atmosphere with a rate of ≈ 1000 particles per square meter per second, is 98 % protons and less than 2 % electrons. The fraction of gamma radiation is only ≈ 0.1 %, but, because of its unique feature, opens an unparalleled window to the universe. While charged cosmic rays loose their information of direction during their propagation towards earth due to magnetic fields, the gamma-rays are not affected and can be used to study the sources of the cosmic radiation. However, gamma-rays are not produced directly by the sources of the cosmic radiation. Instead charged particles are accelerated, which then emit gamma-rays via synchrotron radiation, Π^0 decay and the inverse Compton effect. At the moment, a wide range of VHE source types is known, for example supernova remnants, pulsars, plerions, radio and star burst galaxies. All sources have in common, that the obtained spectra are non thermal, thus allowing the observation of the most violent processes in the known universe. A drawback of gamma-ray astronomy is, that the earth's atmosphere is not transparent for gamma radiation. Due to the significant reduction of the flux with an increase of the particle's energy, space based observatories, with a maximal detection area of $\approx 1\,\mathrm{m}^2$, are not an option to observe the universe with gamma-rays in an energy range above $\mathcal{O}(100\,\mathrm{GeV})$. An alternative solution was shown by Galbraith and Jelly [8], namely the usage of the earth's atmosphere as a detector for the cosmic radiation. High energy particles start to interact and, therefore, loose energy when they enter the atmosphere. The result is the formation of an air shower of particles, see Section 2.1, traveling at a speed faster than light in that medium. One or more telescopes can be used to detect the Cherenkov radiation emitted by these particles, see Section 2.2. Currently the four major Cherenkov telescope systems in use are Cangaroo III, H.E.S.S., MAGIC and Veritas, all of them having multiple telescopes to allow the use of stereoscopy, see Section 2.3.

2.1 Air shower formation

Upon entering the earth's atmosphere, the high energy particles of the cosmic radiation start to interact with the particles of the air. The result is a loss of energy of the primary particle, i.e. the particle of the cosmic radiation which entered the atmosphere. During this process, several new high energy particles (secondary particles) are created, forming a so called air shower. The energy loss mechanism depends on the type of the primary particle, for instance the strong and weak force are responsible for all hadrons. In the case of photons and electrons an electromagnetic shower is formed, with the energy loss due to Bremsstrahlung and pair production. Below a critical energy $E_c \approx 80\,\mathrm{MeV}$ of the secondary particles, ionization

processes with the molecules of the atmosphere start to dominate. Because no new particles are produced when E_c is reached, the corresponding depth in the atmosphere is called the shower maximum. To describe the evolution of the air shower a simple model can be used [9]. It is assumed, that a photon travels a characteristic distance X_0 until it undergoes pair production in the Coulomb field of a nucleus. One electron and one positron are created in this process, each having half the energy of the photon. These two fermions then emit, after traveling the distance X_0, one photon each, because of Bremsstrahlung, and split their energy equally. This corresponds to a doubling of the number of particles N in the shower for each characteristic distance X_0 and can be described as function of the atmospheric depth X:

$$N(X) = 2^{X/X_0} \tag{2.1}$$

Because of the equal splitting of the energy, the mean energy of a particle in the shower is described by:

$$E(X) = E_0 \cdot 2^{-X/X_0} \tag{2.2}$$

Here E_0 is the energy of the primary particle. This leads to the maximum number of particles of:

$$N_{max} = \frac{E_0}{E_c} \tag{2.3}$$

Additionally, the depth of the shower maximum is given by:

$$X_{max} = X_0 \cdot \frac{\log(E_0/E_c)}{\log(2)} \tag{2.4}$$

Although, this is a very simple model of an electromagnetic air shower, the results derived are very similar to the ones obtained through complex Monte Carlo simulations, which can be seen in Figure 2.1 for an electromagnetic and an hadronic air shower. It is obvious, that the distribution of the hadronic shower is considerably wider than the electromagnetic one. This is due to a higher transverse momentum of secondary particles created by strong or weak interactions. Multiple scattering is responsible for the broadening of the electromagnetic shower. However, its cone like shape is preserved and its direction is not altered. The different longitudinal distributions for the different primary particles can be used to suppress the background of hadronic air showers, which occur more often than electromagnetic shower by a factor of $\approx$10.000. This is described in more detail in Section 2.5. The typical air shower lasts for approximately 16 ns and starts in a height between 15 km and 20 km above sea level and the shower maximum is reached at a height of 8 -12 km.

2.2 Cherenkov radiation

If a charged particle travels with a speed v through a medium with the refractive index n, it induces dipoles along its path. These dipoles emit radiation, while they are trying to reach their equilibrium state. If the particle is faster than the speed of light in the medium, i.e.:

$$v > \frac{c}{n} \tag{2.5}$$

with c being the speed of light in vacuum, a constructive interference of the radiation, emitted by the induced dipoles, occurs. This is called Cherenkov radiation and is shown in Figure 2.2.

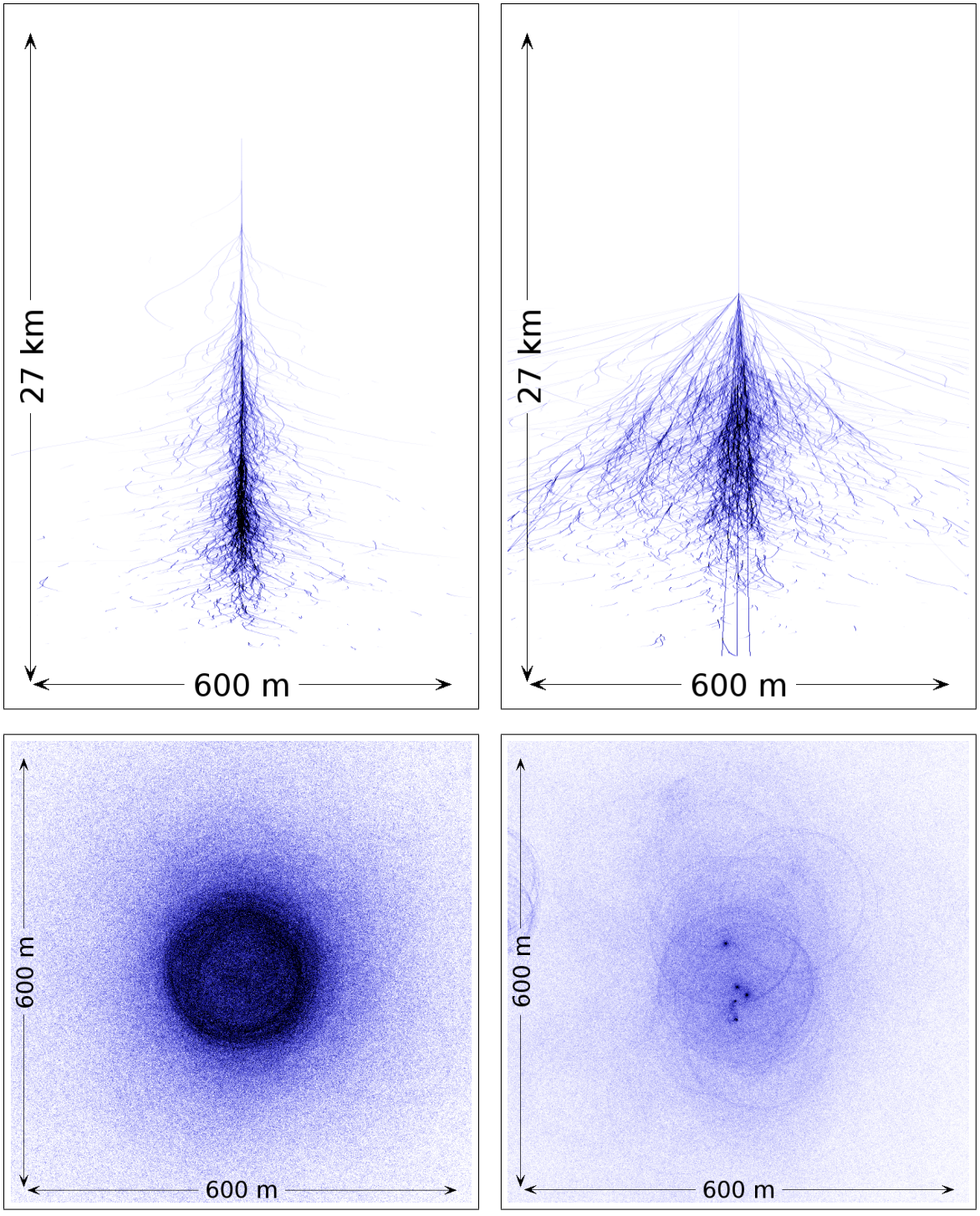

Figure 2.1: *The longitudinal and lateral distribution on the ground of a simulated gamma-ray induced air shower on the left, and a simulated proton induced air shower on the right, are shown. The significantly more spread evolution of the hadronic shower and the development of sub showers in it are clearly visible. This is opposed to the electromagnetic shower, where the direction is not altered. (Courtesy of K. Bernlöhr)*

Each dipole emits a spherical wave, which, following Huygens's principle, creates a wave front similar to the one of supersonic airplanes. The opening angle θ_c of this light cone can be described by

$$\cos(\theta_c) = \frac{1}{n \cdot \beta} \tag{2.6}$$

It depends on the refractive index n of the medium and on the speed of the particle $\beta = \frac{v}{c}$. Taking into account the lateral distribution of the shower and typical opening angles of $\approx 1^\circ$, a circle with a diameter of $\approx 250\,\mathrm{m}$ is illuminated on the ground, see Figure 2.1. For a 1 TeV gamma-ray the typical number of Cherenkov photons reaching the ground is in the order of 100 photons per m^2. Therefore, todays Cherenkov telescopes can only be used in clear moonless nights. The intensity of the Cherenkov radiation emitted by the particles in an air shower is proportional to the negative square of the wavelength of the radiation. Nonetheless, the spectrum of the Cherenkov radiation is modified in the atmosphere, resulting in a peak around $\approx 330\,\mathrm{nm}$.

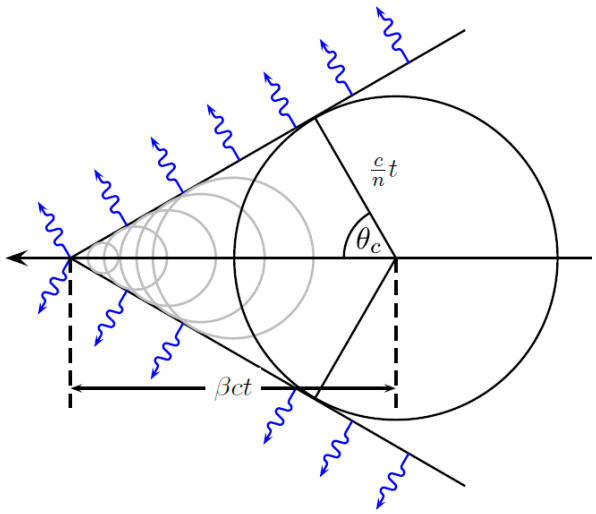

Figure 2.2: *Illustration of the formation of the Cherenkov wave front. The particle traveling faster than the speed of light in the medium with refractive index n induces dipoles. Upon relaxation of those dipoles, spherical waves are emitted, which interfere constructively. The characteristic opening angle θ_c and its dependence of n and β are shown. (Figure taken from [10])*

2.3 Imaging atmospheric Cherenkov technique

In order to use the earth's atmosphere as a detector for cosmic gamma radiation and to identify the sources of this radiation and its attributes, the following information has to be extracted from an air shower:

- the identity of the primary particle to suppress the background.
- the direction of the shower to pinpoint the origin of the gamma radiation.
- the energy of the primary particle to extract a spectrum of the source.

To get these information a two dimensional image of the distribution of the Cherenkov radiation of an air shower is used. A detector, called camera, consisting of several hundred very sensitive photomultipliers (PMT), called pixel, monitors the night sky for the short flashes of Cherenkov light of an air shower. To increase the number of photons, which are seen by the detector, a parabolic or spherical mirror is used. The simulated image of a shower taken by a camera consisting of 960 PMTs is illustrated in Figure 2.3 for a gamma event on the left and a proton event on the right. The elliptical shape of the electromagnetic shower is visible, opposed to the, more or less, random shape of the hadronic shower.

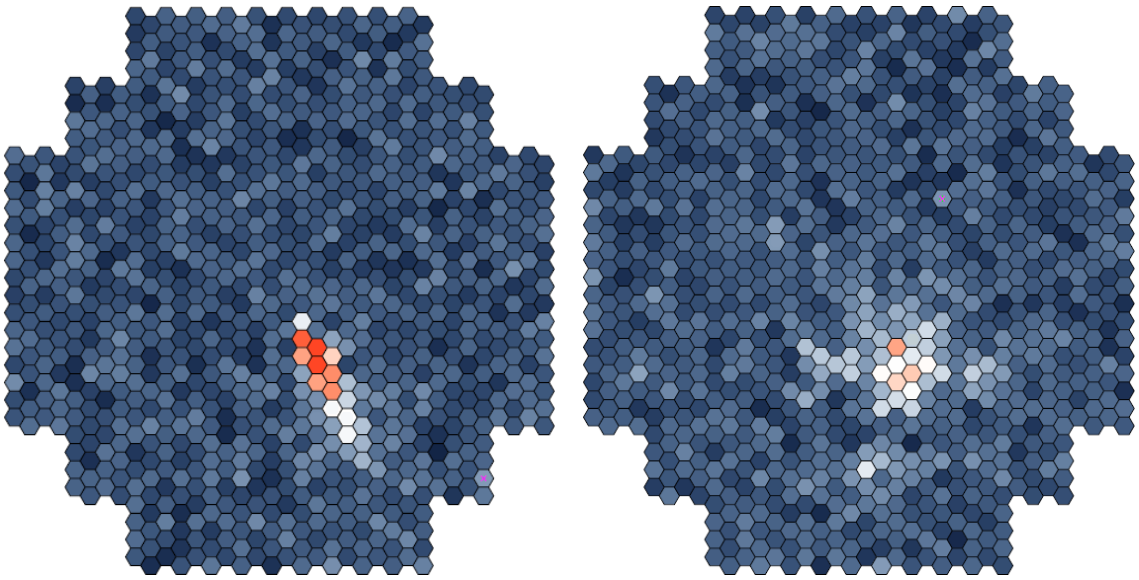

Figure 2.3: *Shown is a simulation of a camera image of a* 1 *TeV gamma-ray shower on the left and a* 0.8 *TeV proton on the right (courtesy of K. Bernlöhr). The different shapes of the two showers can be used to distinguish between different primary particles.*

Stereoscopic observation, where multiple telescopes are placed inside the cone of Cherenkov light of an air shower, offers several improvements for VHE gamma astronomy. For example, the background of local muons, which are created deep in the atmosphere, can be suppressed, if a simultaneous signal in more than one telescope is demanded. This is possible, because muons have a narrow cone of Cherenkov light, thus hitting only one telescope. Furthermore, some hadronic air showers look like electromagnetic showers from one telescope, but can be rejected, using the image of another telescope, which observes the shower under a different angle. Another advantage of stereoscopy is, that basic triangulation can be used to estimate the source position more precisely. Figure 2.4 shows the result, if an gamma-ray induced air shower is seen by four Cherenkov telescopes. The images of the four cameras are superimposed and the Hillas ellipses (see Section 2.4), the shower direction and the source position are marked.

2.4 Hillas parametrization of air showers

In order to extract a set of attributes, which describes all necessary properties of an air shower, out of a camera image, the so called Hillas parametrization is used [12]. As seen in Figures 2.1 and 2.3 the shape of the projection of the Cherenkov light of the shower into

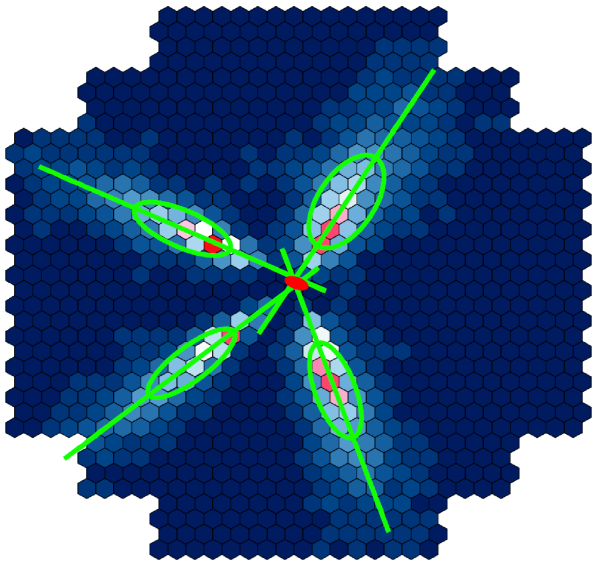

Figure 2.4: *Superposition of the gamma-ray shower images of four cameras. The Hillas ellipses, the shower direction and the source position are marked. The use of multiple telescopes significantly increases the quality of the reconstruction of the shower parameters. (Based on a Figure taken from [11])*

the focal plane of the camera resembles an ellipse. The size, position and orientation of these ellipses, as well as the comprised light intensity, are part of the Hillas parameters. An illustration of this is shown in Figure 2.5. The length of the minor axis, called the *width*, and the length of the major axis, named *length*, are used to define the shape. The radial distance of the *center of gravity* of the ellipse to the camera center is called the *local distance*. The angle between the *local distance* and the major axis of the ellipse is the parameter *alpha* and defines the orientation of the ellipse in the camera. The angle of the shower in the camera is called *theta*. The light intensity inside the ellipse is the *size* or *image amplitude* of the shower.

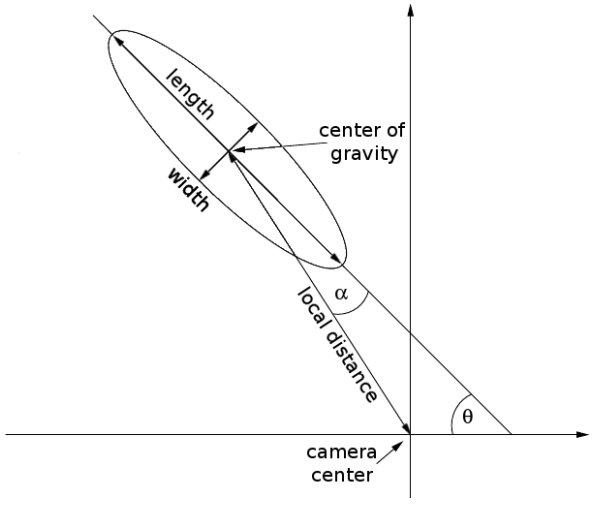

Figure 2.5: *Illustration of the Hillas parametrization of an air shower. The size, position and orientation of the ellipse are used to characterize the camera image. (Based on a Figure taken from [13])*

2.5 Primary particle identification

If the Hillas Parameters are used to exclude the background of hadronic air showers, the first step is the reduction of the noise in the camera images. This is done to get a better estimation of the shape of the ellipses and is achieved through the so called tailcut. The tailcut uses two threshold values to exclude pixels as background and sets their intensities to zero. For example, for a tailcut of 5/10, a pixel has to have at least an intensity of 5 p.e. and a neighbor pixel with an intensity greater than 10 p.e., or vice versa, in order not to be rejected. This can also be seen in Figure 2.4, where only the pixels around the ellipses survived the tailcut. After this procedure is applied to all camera images of a shower, the shapes of the ellipses, characterized by their *length* and *width*, are used to reject hadronic showers. To take the most advantage out of the imaging atmospheric Cherenkov technique (IACT), the reduced scaled mean of the *length* (RSL) and *width* (RSW) are calculated for every telescope by comparing the expected shape of the ellipse, extracted from Monte Carlo simulations, with the actual one:

$$RSW = \frac{width - \langle width \rangle_{MC}}{\sigma(width)_{MC}} \tag{2.7}$$

$$RSL = \frac{length - \langle length \rangle_{MC}}{\sigma(length)_{MC}} \tag{2.8}$$

After that, the weighted mean of the RSW and the RSL of every camera image is calculated, using a weight w_i for RSW_i and a weight l_i for RSL_i for the i^{th} telescope:

$$w_i = \frac{\langle width_i \rangle^2_{MC}}{\sigma^2(width_i)_{MC}} \tag{2.9}$$

$$l_i = \frac{\langle length_i \rangle^2_{MC}}{\sigma^2(length_i)_{MC}} \tag{2.10}$$

The *mean reduced scaled width* $MRSW$ and the *mean reduced scaled length* $MRSL$ for N telescopes is than given by:

$$MRSW = \frac{\sum_{i=1}^{N} w_i \cdot RSW}{\sum_{i=1}^{N} w_i} \tag{2.11}$$

$$MRSL = \frac{\sum_{i=1}^{N} l_i \cdot RSL}{\sum_{i=1}^{N} l_i} \tag{2.12}$$

The standard cuts, used by H.E.S.S. to reject the background of hadronic air showers, are a $MRSW$ between -2.0 and 0.9 and a $MRSL$ between -2.0 and 2.0. This results in an increase of the signal to noise ratio from 1:100 to 1:1 for strong point-like sources.

3 The H.E.S.S. experiment

The High Energy Stereoscopic System (H.E.S.S.) is located near the Gamsberg in the Khomas Highland in Namibia at 23° 16.28′ S 16° 30′ E, at an altitude of 1800 m above sea level, approximately 100 km south west of the capital Windhoek. It consists of four imaging atmospheric Cherenkov telescopes, with a fifth currently under construction. Figure 3.1 shows the layout of the array, the four smaller telescopes are placed on the edges of a square with a side length of 120 m, the bigger H.E.S.S. phase II telescope is situated at the center. This setup is chosen, because the typical radius of the cone of Cherenkov light is $\approx$120 m, see Section 2.2. Therefore, it guarantees that multiple telescopes observe the same Cherenkov event, allowing the use of stereoscopy, see Section 2.3. The area around the Gamsberg is known for its ideal observation conditions, which are:

- a very low humidity.
- an optimal height above sea level to monitor the complete evolution of an air shower.
- many cloudless and moonless nights.
- almost no stray light of human origin.

The H.E.S.S. phase I telescope system is able to detect gamma-rays in an energy range from 100 GeV up to hundred TeV [14]. The upper energy limit is due to the reduction of the flux of the gamma-rays with higher energies. A source, with a flux of 1 % of the Crab Nebula, which is a standard candle in gamma-ray astronomy, can be detected in 25 h of observation with 5 σ significance. The energy resolution is between 15 % and 20 %. With the H.E.S.S. phase II telescope, a significant lowering of the energy threshold to 30 GeV is expected, as well as an increase in sensitivity [15].

Figure 3.1: *Photo of the five H.E.S.S. Cherenkov telescopes. The big dish under construction in the middle belongs to the H.E.S.S. phase II telescope.*

3.1 Telescope dishes and mirrors

The four H.E.S.S. phase I telescopes consist out of a steel construction and use an alt-azimuth mount to track targets in the sky. This allows zenith angles in a range from 0° up to 89.9° and a slew rate of 100° per minute. The dish of every telescope is 13 m in diameter and has a focal length of 15 m [14]. It is built using the Davies-Cotton design [16] and is composed out of 380 circular mirrors with a radius of 30 cm. The resulting effective mirror area is 107 m^2 per telescope. The reflectivity of the mirrors was between 80 % and 90 % at the time of installation. Each mirror facet can be aligned separately using the two motors, which are part of its mounting structure. With this telescope setup, a systematic pointing uncertainty of 0.6″ per axis can be achieved [17]. Figure 3.2 shows a picture of the H.E.S.S. phase I telescope 3 (CT3). Visible is the red steel structure of the telescope itself, the dish with the mirrors and the camera, which is mounted at a distance of 15 m from the dish. Also visible is the white electronic-hut in the front, as well as the camera-hut in the back. The mirrors at the top of the dish are missing due to a mirror exchange, which was done in spring 2010.

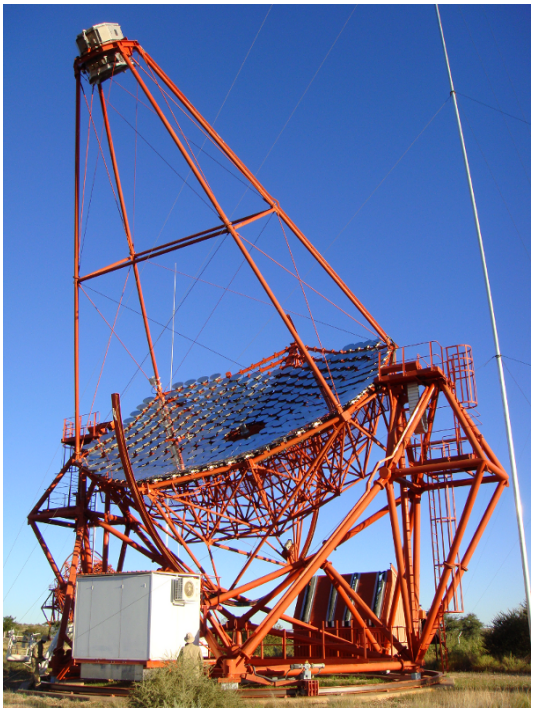

Figure 3.2: *Photograph of the H.E.S.S. phase I telescope CT 3. Visible is the steel structure, the alt-azimuth mount, the dish with its mirrors and the camera. The white hut in the front contains electronics and power supplies. The hut in the back is used to protect the camera from bad weather. Two of the four lightning rods are also visible.*

3.2 Camera layout

The layout of a H.E.S.S. phase I Cherenkov camera can be seen in Figure 3.3. Visible are the 960 Winston cones used to focus the light into the sensitive region of the Photonis XP2960 photomultiplier behind it. Their quantum efficiency has a maximum of about 30 % [18]. Each photomultiplier has a field of view of 0.16°, totaling up to 5° for the whole camera.

The photomultiplier consists of an entry window out of borosilicate glass, eight dynodes and a bialcali cathode. Its features are:

- an after pulse rate of less than 0.025 %.
- a signal rise time of less than 2 ns.
- a possibility to detect single photo electron peaks.
- an amplification of $2 \cdot 10^5$.

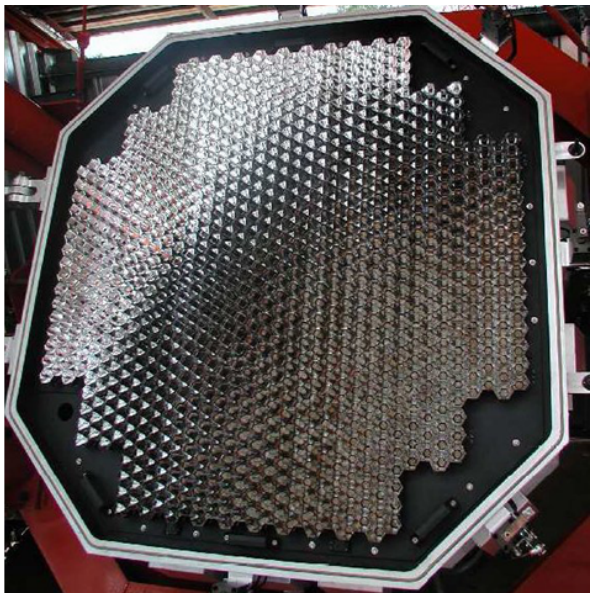

Figure 3.3: *Layout of the camera of a H.E.S.S. phase I telescope. Visible are the 960 Winston cones with the photomultipliers underneath.*

The PMTs are grouped into so called drawers, which consist of 16 photomultipliers each, resulting in a total of 60 drawers per camera. An example of a drawer can be seen in Figure 3.4. Visible are the PMTs, as well as the two analog data acquisition cards and the main board, consisting of the slow-control and the power supply. The slow-control card is responsible for handling the data stored by the data acquisition cards and monitoring the PMTs. Furthermore, it controls all the necessary settings of the data taking.

Figure 3.4: *Photo of a drawer of a camera. Visible are the 16 PMTs and the corresponding electronics.*

The analog acquisition cards consist of four ARS0 analog ring sampler (ARS) each, developed for the ANTARES neutrino telescope [18]. Each ARS chip can store the data of one amplifier,

called gain channel, for four pixels. They sample the incoming data at a rate of 1 GHz and buffer it in four 128 storage segments, each 1 ns long. Figure 3.5 shows how the ARS operates. New data is written into the segments of the ARS counter clockwise. If the read out of the camera is triggered, which takes about ≈ 70 ns from the signal itself until the trigger signal is sent, the storage segments containing the signal have to be read. Therefore, no more signals are written into the ARS, instead the current segment position is shifted by a time value of $128\,\text{ns} - n_d\,\text{ns}$. Now, the current storage segment is at the beginning of the signal and n_f segments are read out, corresponding to a signal length of n_f ns. The correct values for n_f and n_d are explained in Section 4.1.

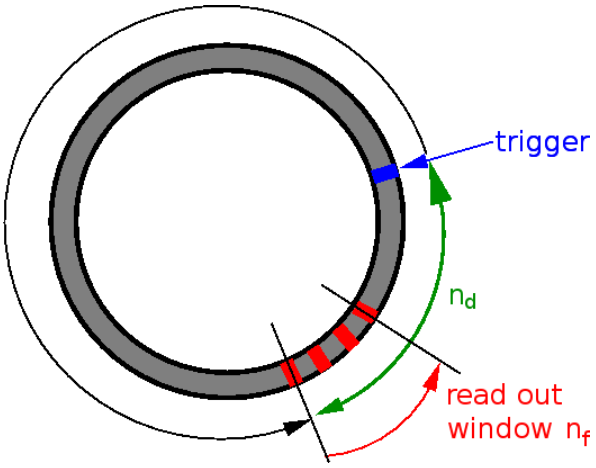

Figure 3.5: *Illustration of the mode of operation of an analog ring sampler. The time between the Cherenkov signal and the trigger signal are n_d ns, the length of the Cherenkov signal is n_f ns.*

A schematic of the camera electronics can be seen in Figure 3.6. If a photon enters the PMT, the photo effect converts it into an electron, which is then multiplied by the dynodes, using the high voltage (HV) of more than 1000 V. The resulting signal is divided between two amplifiers, one for the low, and one for the high intensity signals. These two gain channels are named accordingly the HighGain and the LowGain. The analog ring sampler is used to buffer the data. If a trigger signal is received, the ARS is read out. This can be done in charge mode, where the integrated signal over the time period n_f is returned, or the sample mode, where each 1 ns segment of the time period n_f is read out separately. The signal is then converted, from an analog to a digital signal, by an ADC and send to the data acquisition to be written to disk. With these camera electronics an event rate of ≈ 1 kHz is possible.

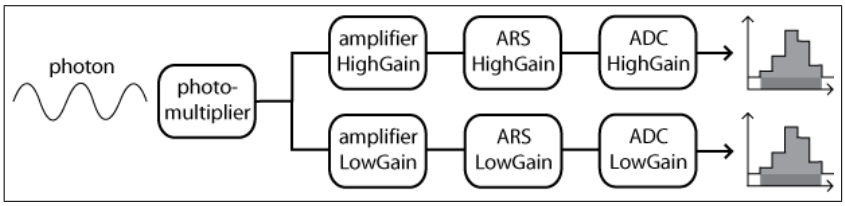

Figure 3.6: *Schematic of the camera electronics. The photomultiplier signal is send into two different amplifiers. The amplified signal is stored in an ARS for both channels. If a camera readout is triggered, a signal, if wanted, integrated over* 16 *ns, is read out and converted, from analog to digital, by the ADC.*

4 Camera calibration

With the recent detection of several weak TeV gamma-ray sources, as stated in Chapter 1, a detailed understanding of the camera calibration is essential. In order to reconstruct the direction, shape and energy of an air shower the signal of each photomultiplier gain channel, called raw data, must be converted into a pixel intensity comparable for all cameras. The typical calibration procedure is discussed in the following.

4.1 Readout window of the analog ring sampler

As explained in Section 3.2, the cameras use analog ring samplers to store the last 128 ns of raw data. To ensure a correct readout of the cameras, the time between the Cherenkov event and the trigger signal n_d, and the length of the readout window n_f, have to be determined. For n_f the following criteria apply:

- The Cherenkov signal has to be fully contained in the readout window.
- The readout window has to be as small as possible to reduce the contamination of the signal with night sky background and electronic noise.

Considering these criteria, the n_f value is set to 16 ns. Figure 4.1 shows the readout window of a pixel for three Cherenkov signals. Most of the signals are similar to the two seen on the right. They are well contained in the read out window and the n_f value is validated because of this. The signal on the left is an example of a signal, which is not read out correctly.

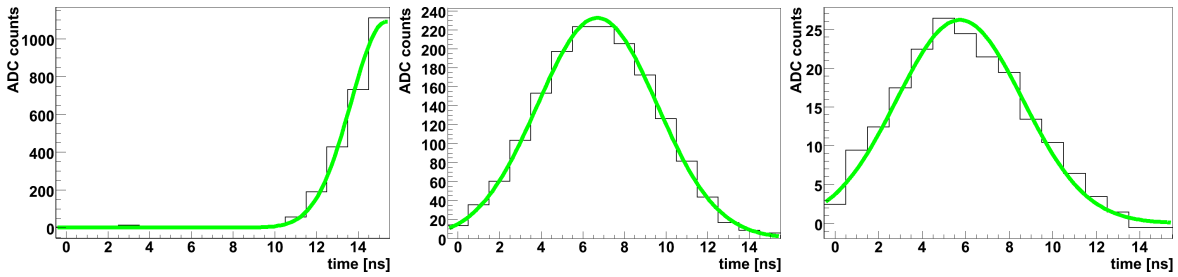

Figure 4.1: *Shown are three Cherenkov signals in the read out windows of three different pixels with the corresponding Gaussian fit. The left signal is cut off and not read out correctly. The other two are fully contained in the readout window and no additional night sky background, at the beginning or the end, are read out. The result is an optimal signal to noise ratio.*

The time n_d between the trigger signal and the Cherenkov signal itself depends on the transit time of each photomultiplier and therefore on the HV of the PMT. Because the n_d value can only be set for one drawer, the PMTs of each drawer are selected to limit the high voltage variations to less than 70 V. This corresponds to a negligible transit time difference of $\approx$ 1.3 ns. To verify the setup of the n_d values, a set of six sample mode observation

runs on the Crab Nebula were taken in November 2009. To obtain an overview about the behavior of the whole camera, a fit was performed to the signal distributions. In detail, the signal in the readout window was determined by a Gaussian to obtain the position of the peak and the width of the signal. Although the signal is not symmetric, the Gaussian fit was chosen, because it is easy to use and produces stable results. Furthermore, most of the signals are described very well by a Gaussian and the accuracy of the resulting peak positions and widths are sufficient for this study. All the Cherenkov signals in the pixels of a camera, which survived a tailcut, where fitted. This was done for every event of the six sample mode runs. The resulting distributions for the fitted signal peaks and the σ of the Gaussian fits can be seen in Figure 4.2 for telescope 1 (CT1). Almost all signals are contained in the readout window.

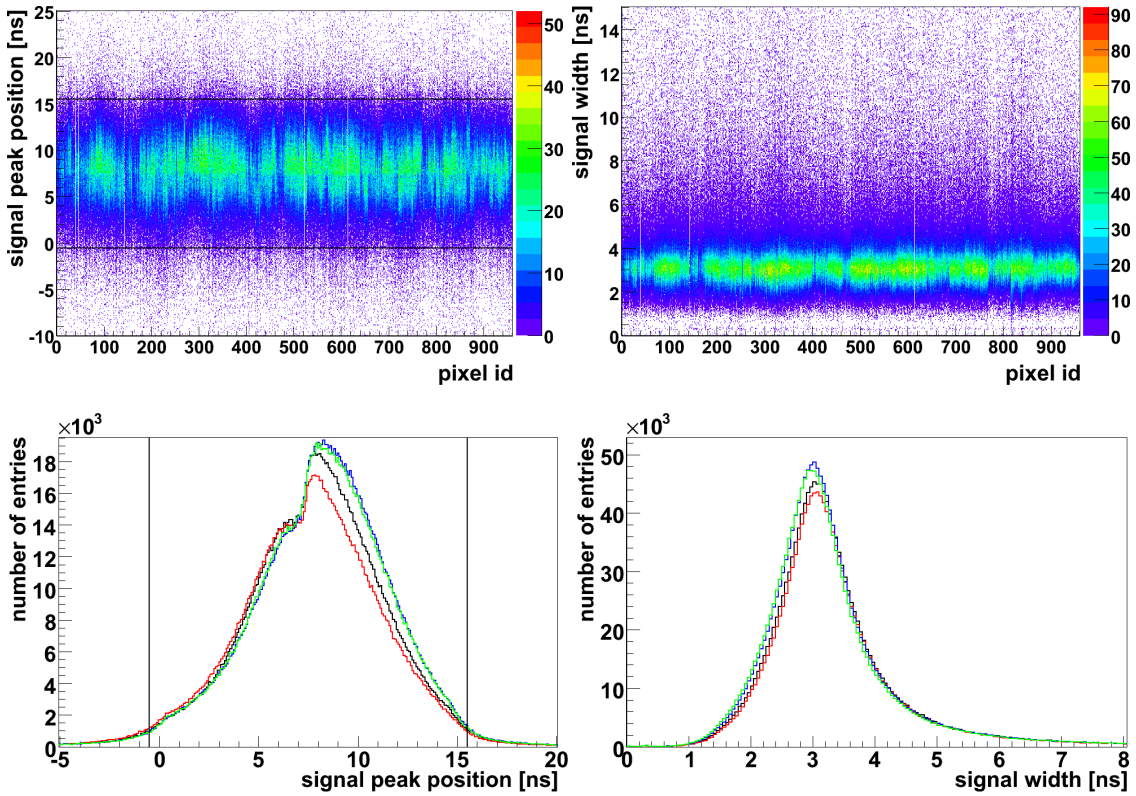

Figure 4.2: *Overview of the signal positions in the readout windows before the camera recalibration. In the upper left, the distribution of the peaks of the signal as a function of the pixel id for CT1 is shown, in the upper right, the σ of the Gaussian fit is plotted. The lower Figures show the projections of the whole camera for all four telescopes. Only signals with an intensity between 1 p.e. and 100 p.e. have been used. CT1 is drawn in black, CT2 in red, CT3 in blue and CT4 in green. The two straight black lines in the Figures on the left indicate the boundaries of the read out window.*

In spring 2010 the cameras were recalibrated and Figure 4.3 shows the change in the signal distributions. To control the recalibration, sample mode runs were taken, where the cameras were illuminated homogeneously. This was done using the single photo electron unit (see Subsection 4.2.2), resulting in pixel intensities between 1 p.e. and 100 p.e. The fitted signal peak positions and signal widths are shown in Figure 4.3. The width of the distributions is smaller than the one obtained through observation runs, because there are no aberration

effects of the mirrors. For further details see Subsection 4.1.3 or [19]. Furthermore, the photon arrival times for all pixels are the same for the homogeneous illumination, opposed to the spread in the arrival times for a Cherenkov event. The pixels with unusual wide peak and σ spreads in Figure 4.3 suffer from an ARS readout problem, see Section 4.3, and are not included in the projection plots. The strange behavior of CT3, i.e. the significant smaller number of events, is due to a readout problem of the camera.

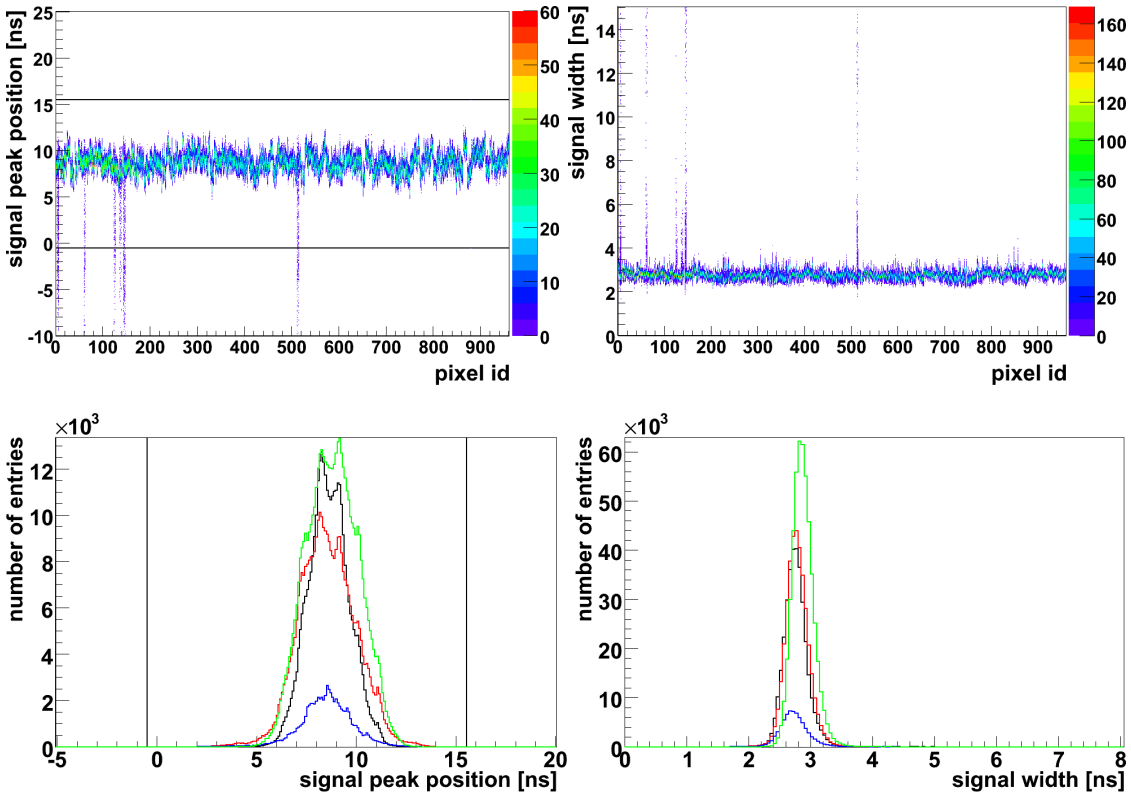

Figure 4.3: *Overview of the signal positions in the readout windows after the camera recalibration. In the upper left, the distribution of the signal peaks as a function of the pixel id for CT1 is shown, in the upper right, the σ of the Gaussian fit is plotted. The lower Figures show the projections of the whole camera for all four telescopes. Only pixel with an intensity between 1 p.e. and 100 p.e. have been used. Pixels with an ARS problem are not included in the projection plots. CT1 is drawn in black, CT2 in red, CT3 in blue and CT4 in green. The boundaries of the read out window are shown in the plots on the left side as two straight black lines.*

4.1.1 Pixel amplitude dependencies

To investigate a possible shift of the signals with increasing pixel intensity, the data was divided into samples of different pixel intensities and *image amplitudes*. For this study 6 sample mode observation runs on the Crab Nebula taken in November 2009 were used. Figure 4.4 shows, that there is a small shift to higher values of the signal peak position. It depends on the increase of the image amplitude. No other dependencies are visible.

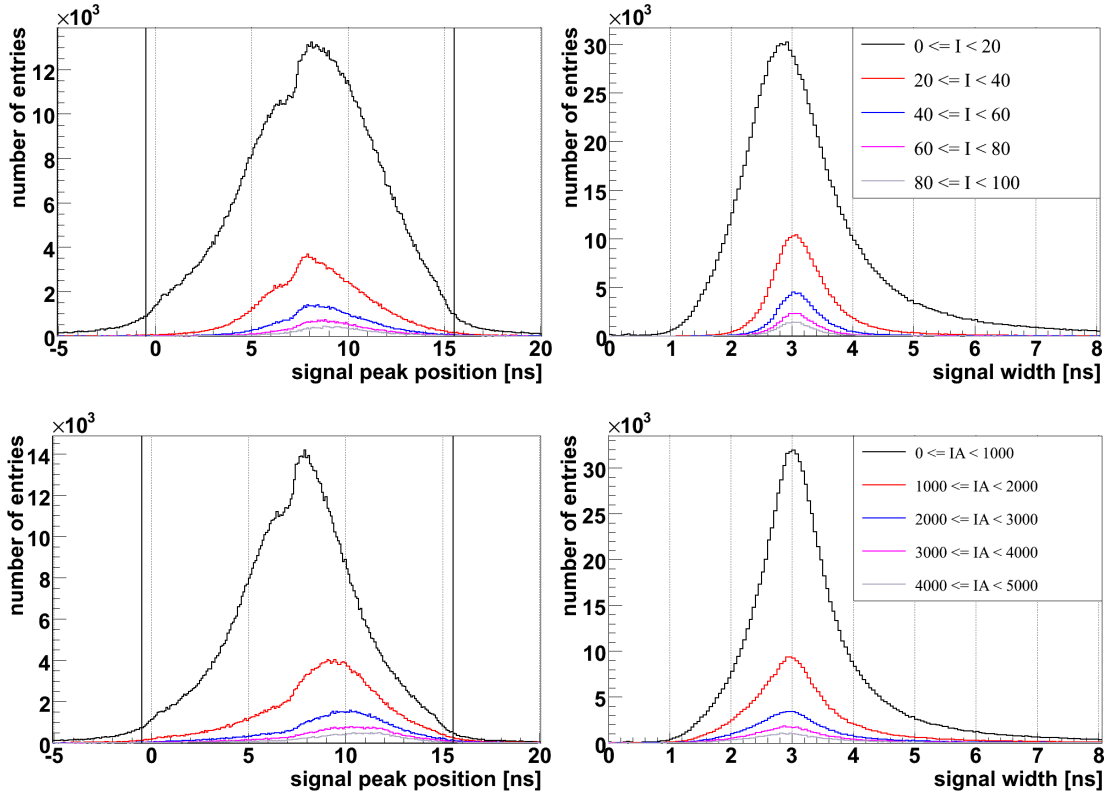

Figure 4.4: *In the upper left, the projection of the signal peak distribution for different intensity cuts is shown for a complete camera. In the upper right, the σ of the Gaussian fit is plotted. In the lower row, different image amplitude cuts have been applied. The two straight black lines in the Figures on the left side are the boundaries of the read out window. Only a mild shift in the signal peak distribution for higher image amplitudes is visible.*

4.1.2 Shower energy dependencies

Additionally, the distributions of the signal peak and width as a function of the shower energy have been studied. The result is shown in Figure 4.5 and should be similar to the *image amplitude* dependency. The width of the signal is not influenced by an increase in the energy of the primary particle. As expected, the peak position of the signal is getting shifted forward in time with higher shower energies. Nonetheless, the change in the distribution is not effecting the validity of the parameters n_d and n_f.

4.1.3 Pixel position dependencies

To check for the influence of the position of the pixel in the camera on the parameters n_d and n_f, the distance of the *center of gravity* of the shower to the camera center, the so called *local distance*, is used. Expected are aberration effects of the mirrors and a larger number of events with increasing distance to the camera center, due to a bigger detector volume. Figure 4.6 shows, that there is no significant influence of the local distance on the signal peak and width distributions. The broadening of the distributions in the outer regions of the camera is because of the aberration effects of the mirrors of the telescope, which gets worse with the offset to the focus. As stated in [19], the signals are spread over an interval of up

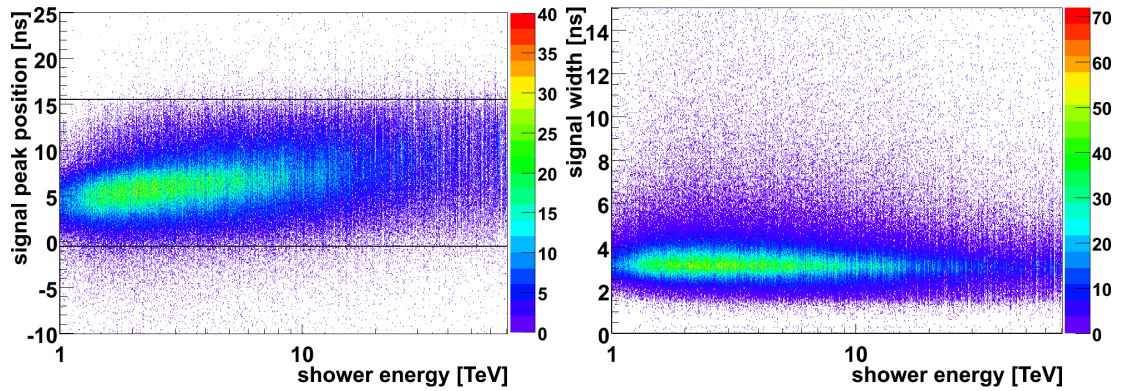

Figure 4.5: *On the left, the signal peak distribution as a function of the shower energy is shown, on the right, the σ of the Gaussian fit is plotted. The boundaries of the read out window are shown by two straight black lines in the plot on the left. A shift of the signal peak position forward in time with an increase of the energy of the primary particle is visible. Nonetheless, it is not big enough to be significant.*

to 5 ns with an RMS of 1.4 ns. The build up of the arriving time offset to 5 ns can clearly be seen in the left plot of Figure 4.6. An increase in the RMS of the signal width of about 1.4 ns is visible in the right plot.

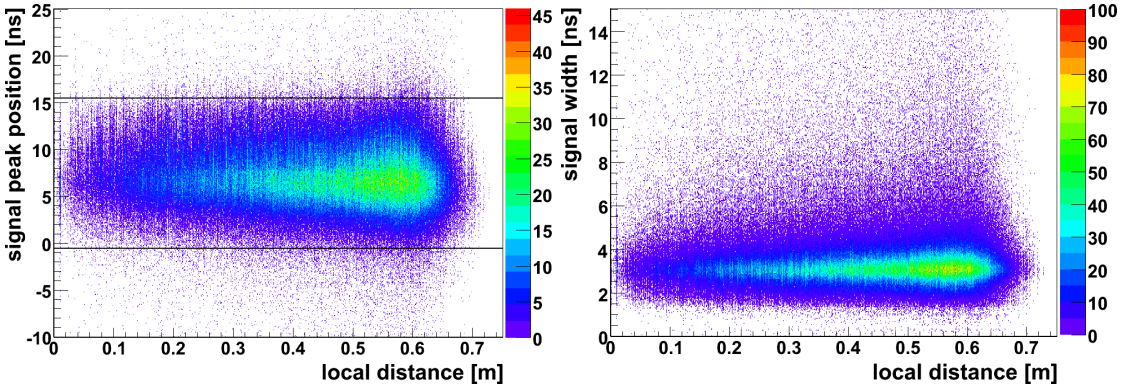

Figure 4.6: *On the left, the signal peak distribution as a function of the local distance is shown, on the right, the σ of the Gaussian fit is plotted. The two straight black lines in the plot on the left are the boundaries of the read out window. No influence of the local distance is visible. The increase in events is due to a bigger detector volume and the smearing because of aberration effects of the mirrors.*

4.1.4 Shower distance dependencies

At last, a possible influence of the distance of the impact point of the shower to the telescopes on the the arrival time has been checked. Figure 4.7 shows, that no dependency of the parameters n_d and n_f on the shower distance exists.

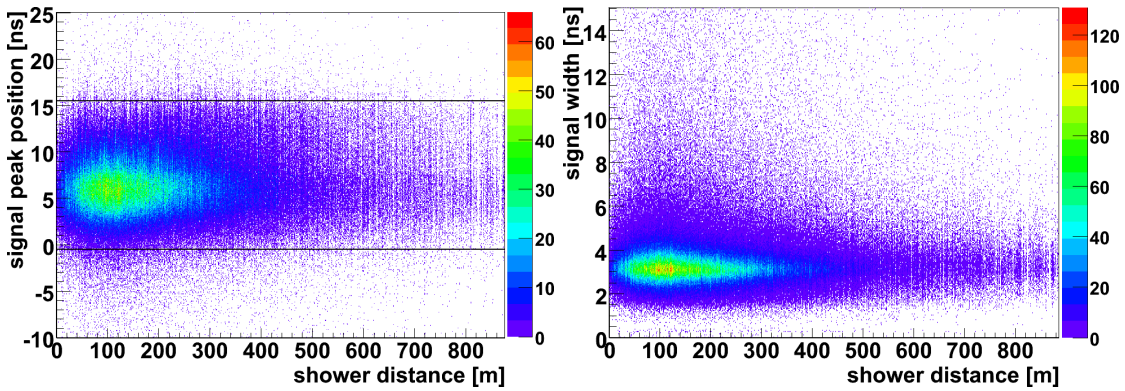

Figure 4.7: *On the left side, the distribution of the signal peak position as a function of the shower distance is visible and the two straight black lines indicate the boundaries of the read out window. On the other side, the corresponding plot for the signal width is shown. No influence of the shower distance on the signal peak position or its width are apparent.*

4.2 Calibration procedure

The goal of the calibration of the cameras is the conversion of the ADC counts of a given pixel to a corrected pixel intensity in photo electrons. This pixel amplitude is then used as a starting point for all further analysis of the shower parameters. The necessary steps to obtain this goal will be presented below.

4.2.1 Converting ADC values to photo electron intensities

The intensity of a given pixel for both gain channels can be calculated using the following equations:

$$I^{HG} = \frac{ADC^{HG} - P^{HG}}{\gamma_e^{ADC}} \cdot \gamma^{FF} \tag{4.1}$$

$$I^{LG} = \frac{ADC^{LG} - P^{LG}}{\gamma_e^{ADC}} \cdot \frac{HG}{LG} \cdot \gamma^{FF} \tag{4.2}$$

Here HG and LG represent the two different gains and ADC is the signal of the photomultiplier in ADC counts in the given channel. P^{HG}/P^{LG} are the pedestal positions or baselines of the HighGain/LowGain channel. The ADC to p.e. coefficient γ_e^{ADC} is the gain of the HighGain channel and is given in ADC counts per photo electron. Because the gain for the LowGain channel can't be determined, see Subsection 4.2.4, γ_e^{ADC} is also used for this channel. However, it has to be multiplied with the amplification ratio $\frac{HG}{LG}$. Finally, the differences in optical and quantum efficiency of the pixels have to be corrected, using the flatfield coefficient γ^{FF}. To obtain a single intensity for each pixel, the values of the two gain channels have to be merged. The HighGain channel is used exclusively up to 150 p.e. and the LowGain channel above 200 p.e. In between, the intensities have to be weighted accordingly and are given by:

$$I = (1 - \epsilon) \cdot I^{HG} + \epsilon \cdot I^{LG} \tag{4.3}$$

where $\epsilon = (I^{HG} - 150\,\text{p.e.})/(200\,\text{p.e.} - 150\,\text{p.e.})$ [20].

The reason for this is seen in Figure 4.8, where the signal in p.e. of the HighGain channel as a function of the signal in p.e. of the LowGain channel is plotted. The saturation of the HighGain channel is easy to see and explains why it is just used up to 200 p.e. The LowGain could be used with intensity as low as 10 p.e. (this is not visible in Figure 4.8). However, a better result is expected, if just the HighGain is used up to 150 p.e.

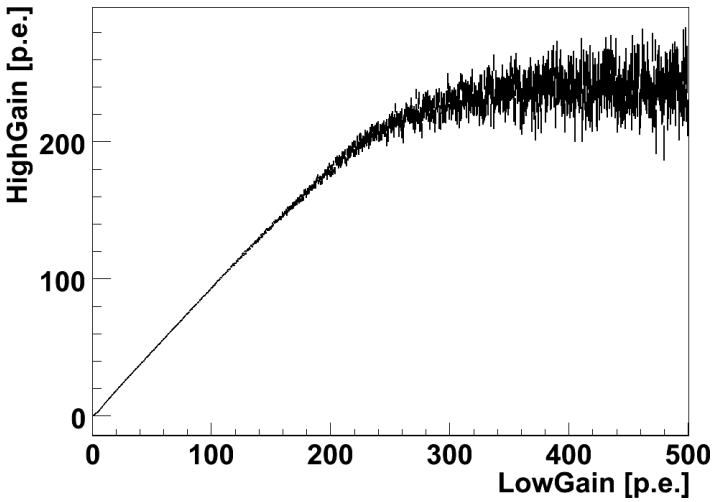

Figure 4.8: *HighGain intensity in p.e. as a function of the LowGain intensity in p.e. The saturation of the HighGain channel is clearly visible.*

4.2.2 Calibration devices

Two determine the γ_e^{ADC} coefficient and the γ^{FF} coefficient two different calibration devices are used. Their location on the telescopes, as well as a short description of their function, will be given now:

- Single photo electron unit
  The single p.e. units are used for the determination of the γ_e^{ADC} coefficients through the measurement of the position of the single photo electron peaks, see Subsection 4.2.4. They are located inside of the camera hut, seen in the back of Figure 3.2, because no night sky background should be present during the determination of the γ_e^{ADC} coefficients. The single photo electron units consists of a LED pulser and a diffuser and they are mounted 2 m away from the camera fronts. The cameras are illuminated with short flashes of light to create intensities between 1 p.e. and 100 p.e. at a rate of 70 Hz [20]. A light intensity homogeneity over a camera of 50 % is achieved.

- Flatfield unit
  The flatfield units are used to determine the γ^{FF} coefficients and should illuminate the cameras as homogeneously as possible, see Subsection 4.2.6. For this, several LED flashers are mounted on the telescope dishes, 15 m away from the cameras. They produce short pulses with an uniform illumination out to 10° [20], which is bigger than the field of view of the cameras. The pulses from the flashers have a FWHM of 5 ns and create intensities between 10 p.e. and 200 p.e. in the pixels.

4.2.3 Pedestal estimation

The mean signal in ADC counts of a given channel of a photomultiplier, without the presence of Cherenkov light, is called the pedestal position. The two main contributions are the electronic noise of the photomultiplier itself and the night sky background. The pedestal position is between -11000 ADC counts and -13000 ADC counts for both channels. The electronic noise is responsible for the pedestal width of about 16 ADC counts in the HighGain and 6 ADC counts in the LowGain channel. Figure 4.9 shows such a pedestal distribution for a single pixel. This is called a dark pedestal distribution, because the camera lid is closed and the HV is turned on. Therefore, only electronic noise is read out. The LowGain peak around -11550 ADC counts corresponds to a baseline of ≈ -730 ADC counts in every 1 ns interval of the readout window. This is equivalent to a baseline voltage of approximately -0.9 V, using a conversion factor between voltage and ADC counts of 1.22 mV/ADC count.

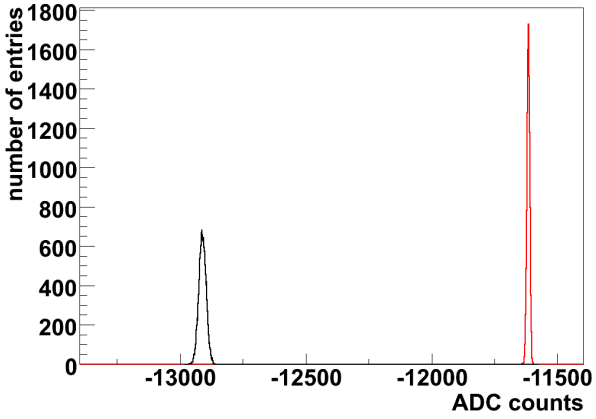

Figure 4.9: *ADC distribution for a photomultiplier, with closed camera lid and activated HV, for both amplification channels. The HighGain is plotted in black and the LowGain in red.*

An average additional increase of over 1 p.e. of the width of the dark pedestal distribution is due to the night sky background. Because of this, an accurate determination of the pedestal position is necessary. During data taking ≈ 200 camera images are recorded every second for every camera. About $\mathcal{O}(10)$ pixels of each camera are contaminated by Cherenkov light, thus the rest of the pixels can be used to determine the pedestal positions. For a detailed description of this procedure see Chapter 5.

4.2.4 ADC to photo electron coefficient

The ADC to photo electron coefficient γ_e^{ADC} represents the position of the signal in ADC counts, a single photo electron would produce in the HighGain channel of a photomultiplier. To obtain it, dedicated runs are taken frequently during each observation period. In those runs, the photomultipliers are illuminated with a weak light source to create single photo electron signals. The ADC distribution of such a pixel can be seen in Figure 4.10.
In case of the LowGain channel, the single p.e. peak can not be resolved, because it is shifted into the pedestal peak. For this reason, an γ_e^{ADC} coefficient can't be determined. To extract a γ_e^{ADC} coefficient from Figure 4.10, a fit is applied with the following assumptions. The distribution consists of a Gaussian pedestal peak and additional peaks for $1, 2, 3, \ldots, n$ p.e. signals, which all are described by a Gaussian too. Furthermore, the number n of photo

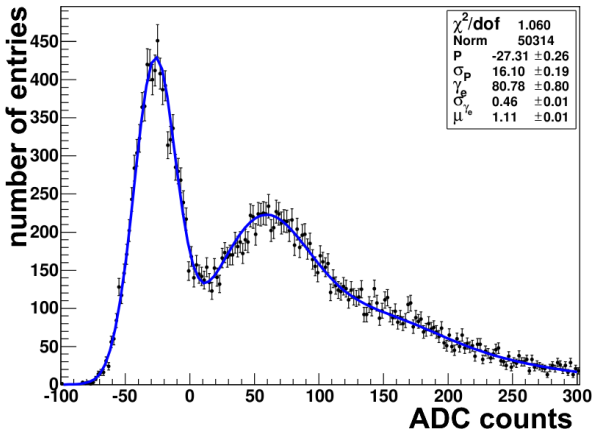

Figure 4.10: *ADC distribution of a single photo electron illumination of a photomultiplier for the HighGain channel. The large peak is the pedestal peak, the second peak and its tail are due to the* $1, 2, 3, \ldots, n$ *p.e. signals. (Figure taken from [20])*

electrons is assumed to follow a Poisson distribution. The photomultiplier response function is than given by [20]:

$$S(x) = N \cdot \left(\frac{e^{-\mu}}{\sqrt{2\pi}\sigma_P} exp\left[-\frac{1}{2}\left(\frac{x-P}{\sigma_P}\right)^2 \right] + \kappa \sum_{n=1}^{m\gg 1} \frac{e^{-\mu}}{\sqrt{2\pi}\sigma_{\gamma_e}} \frac{\mu^n}{n!} exp\left[-\frac{1}{2}\left(\frac{x-\left(P+n\gamma_e^{ADC}\right)}{\sqrt{n}\sigma_{\gamma_e}}\right)^2 \right] \right) \quad (4.4)$$

With

- N as the overall normalization.
- μ as the mean light intensity.
- P as the position of the pedestal peak in ADC counts.
- σ_p as the standard deviation of the Gaussian of the pedestal peak.
- κ as the normalization of the photo electron peaks.
- n as the number of photo electrons responsible for the peak.
- γ_e^{ADC} as the conversion factor between ADC counts and photo electrons.
- σ_{γ_e} as the RMS of the charge induced by a single photo electron.

4.2.5 HighGain to LowGain ratio

Because the γ_e^{ADC} coefficient can't be determined for the LowGain channel, the amplification ratio of the two gains has to be obtained. This is done by plotting the ratio of the ADC counts of the two channels for Cherenkov signals. Because the two gain channels are only comparable in their overlapping linear range of operation, the intensity of a pixel has to be between 30 p.e. and 150 p.e. to be used for this calculation, see Figure 4.8. Figure 4.11 shows a typical HighGain to LowGain ratio distribution for a single pixel. The average ratio for all pixels of the four cameras is around 13.5 with an RMS of ≈ 0.5.

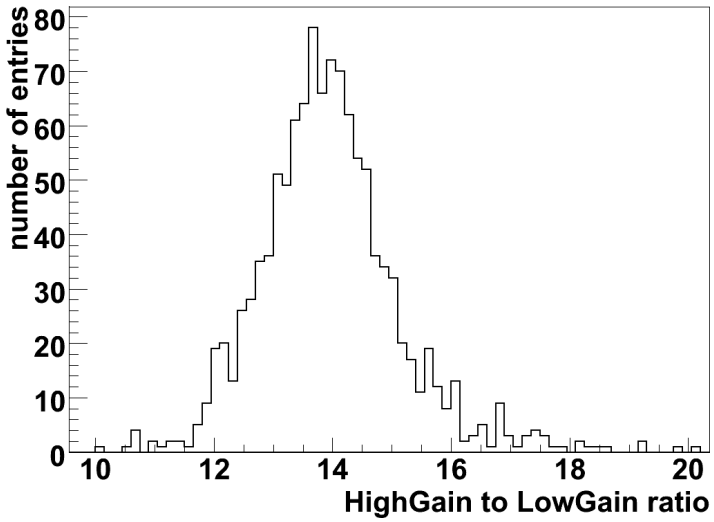

Figure 4.11: *Ratio of the HighGain and LowGain channel for Cherenkov events with an intensity between* 30 *p.e. and* 150 *p.e. for a single pixel.*

4.2.6 Flatfielding

To correct for different optical and quantum efficiencies of the PMTs, dedicated runs, with an homogeneous illumination of the whole camera, are taken. The mean of the signal for every event in the camera is then calculated and the ratio of the pixel intensity to the camera mean is stored in a histogram. The mean of this distribution is the efficiency of the pixel relative to the camera mean. The inverse value is used as the flatfield coefficient. Figure 4.12 shows an example of a flatfield distribution for a whole camera.

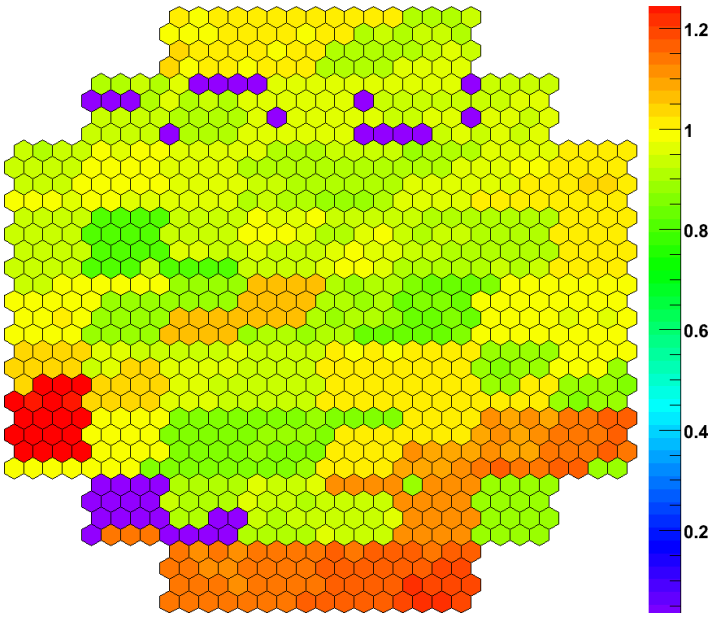

Figure 4.12: *Example of a flatfield coefficient distribution for a single camera. No flatfield coefficients could be derived for pixels with a value of zero, instead the default flatfield coefficient of 1 will be used.*

4.3 Examples of unusable pixels

For a correct reconstruction of the shower parameters, any pixels with abnormal behavior, so called broken pixels, have to be excluded from further analysis. Listed below are the most common examples of pixels which are considered as broken.

1. Dead or deactivated pixel
   If a bright light source illuminates the camera, the photomultipliers are automatically shut down to prevent any hardware damage. In addition to that, hardware problems can lead to pixels with no, or almost no, raw data for a given run. These pixel can easily be identified, as seen in Figure 4.13. If four pixels with consecutive ids are broken, it is most likely that the analog ring sampler has a problem. For 16 consecutive pixels the drawer containing the pixels is the reason.

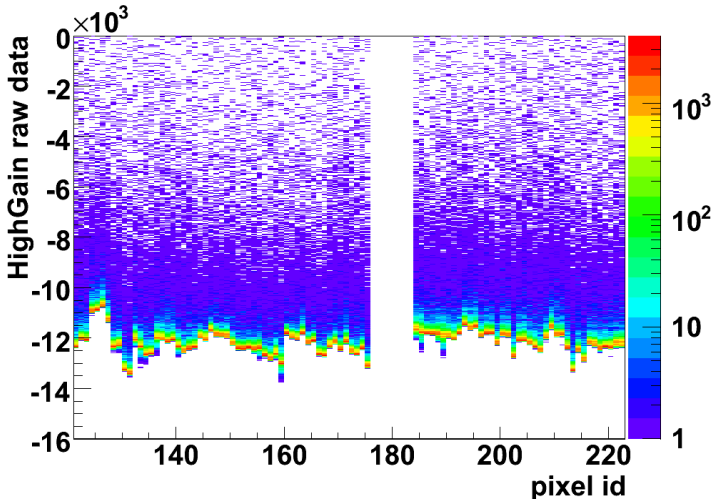

Figure 4.13: *Raw data in ADC counts as a function of the pixel id for a part of a camera for the HighGain channel. Pixel with missing raw data can be easily identified through gaps in the camera distribution.*

2. ARS problem
   Most of the times, the majority of broken pixels are those with an unlocked analog ring sampler. Here the n_d value is set to a random value and most of the time background signals are read out. Characteristic of this problem is, that four pixels in a row are affected in one of the gain channels. The reason for this is, that a single ARS is responsible for one gain channel of four pixels. The ARS problem occurs randomly and is not persistent. Meaning, that every ARS has a small chance to be effected by an unlock with every reconfiguration of the camera electronics. Sample mode runs with a homogeneous illumination of the whole camera, with intensities between 1 p.e. and 100 p.e., have shown a great potential to discover pixel with an ARS problem, as seen in Figure 4.3. Another possibility is, to check the ratio of the gain channels, as described in Section 4.2.5, for unusual high RMS. An example is shown in Figure 4.14.

3. Noisy pixel
   Pixel with an abnormal high rate of signals are called noisy pixels. This is again due to hardware problems. Figure 4.15 shows the distribution of the number of consecutive

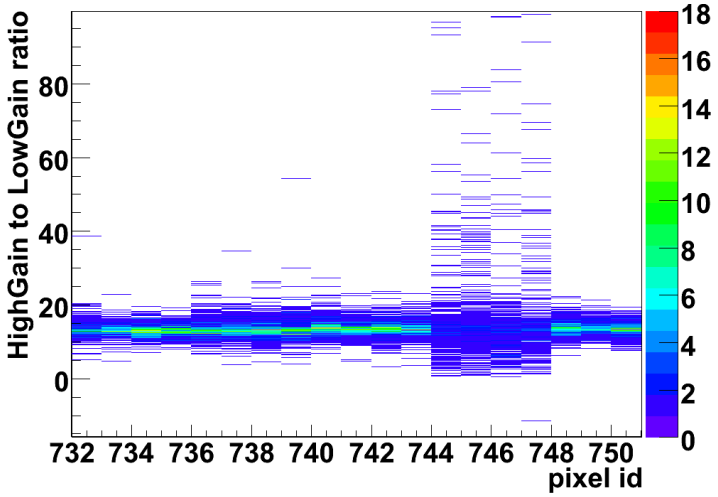

Figure 4.14: *Ratio of the two gain channels as a function of the pixel id. Characteristic of an ARS problem is the unusual wide and deformed distribution.*

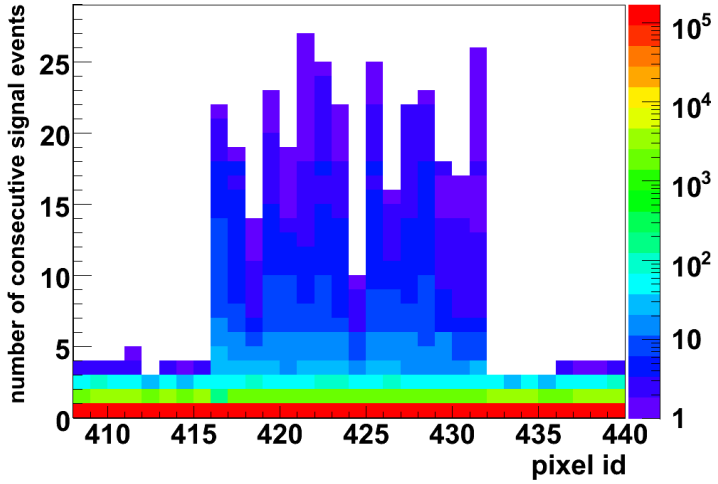

Figure 4.15: *Distribution of the number of consecutive signal events as a function of the pixel id. Noisy pixel have a significant higher RMS and thus can be easily identified, in this case a complete drawer.*

signal events as function of the pixel id. Noisy pixel can easily be identified by an high RMS. In this case a whole drawer is considered noisy.

4.4 Evolution of calibration coefficients over time

With the very long exposure times of the weak TeV gamma-ray sources, mentioned in Chapter 1, of around $\mathcal{O}(100\,\mathrm{h})$ accumulated over several years, the stability of the camera calibration has to be closely monitored. Figure 4.16 for example, shows the evolution of the mean γ_e^{ADC} coefficient for all four cameras over the whole lifetime of the H.E.S.S. experiment. A decrease of the amplification of the photomultipliers with time is clearly visible. To correct for this, the HV of the PMTs is increased from time to time, visible as jumps in the γ_e^{ADC} evolution.
To get an estimation of the evolution of the homogeneity of a Cherenkov camera, the distri-

bution of the flatfield coefficients for each calibration period was fitted with a Gaussian. The mean of this distribution is expected to be around 1, by definition of the flatfield coefficient. The RMS can be interpreted as the inhomogeneity of the camera for the calibration period. In Figure 4.17 the evolution of the inhomogeneity for all four cameras can be seen. It is stable around $\approx 11\,\%$.

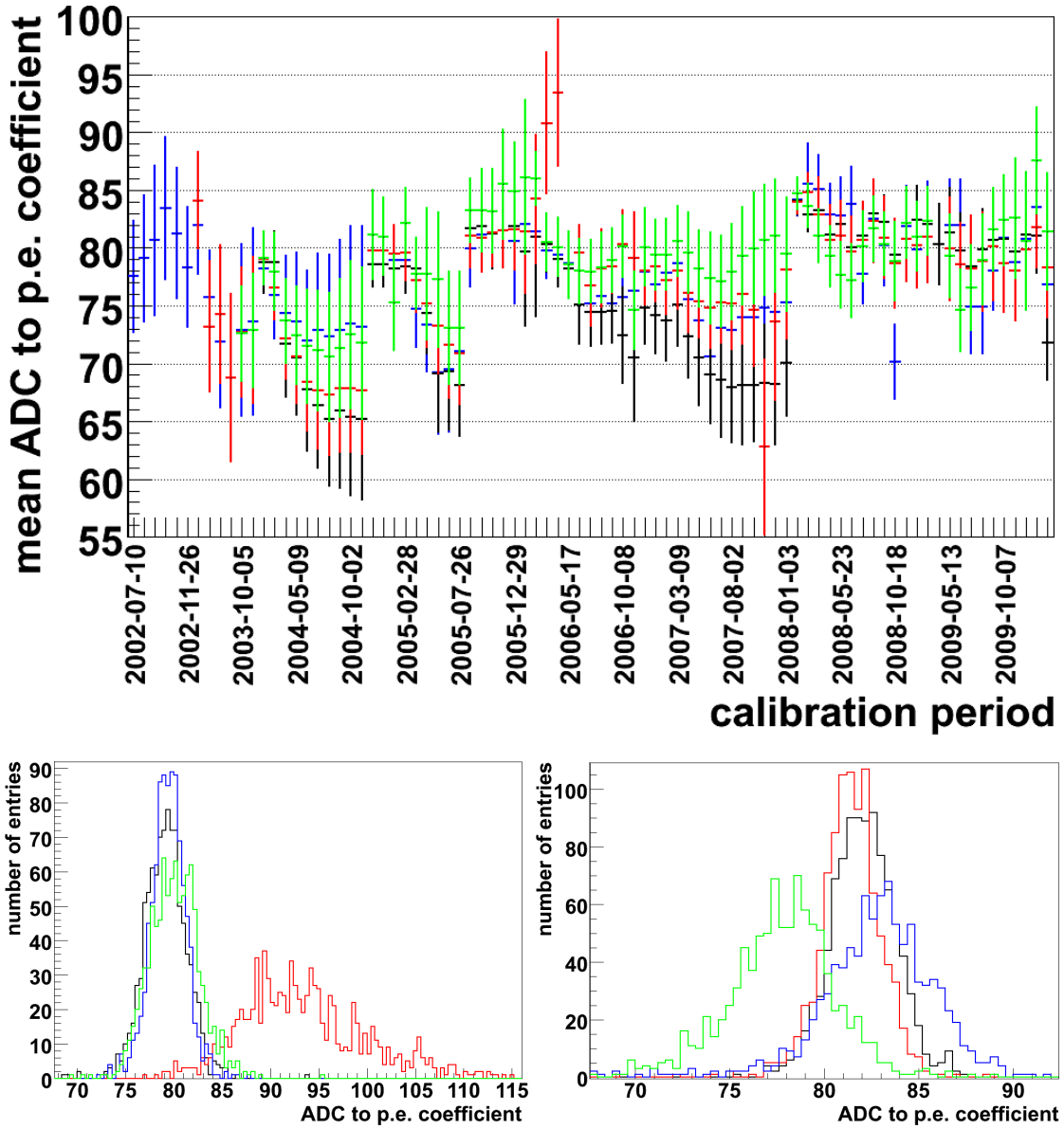

Figure 4.16: *The evolution of the mean γ_e^{ADC} coefficient over the whole lifetime of the H.E.S.S. experiment is shown in the upper row. CT1 is drawn in black, CT2 in red, CT3 in blue and CT4 in green. In the lower row the distributions of the γ_e^{ADC} coefficients for two different calibration periods are plotted. The same color coding as in the upper plot is used. The distributions on the left are for the calibration period starting at the 24.4.06. A problem with CT2 is easy to see. The distributions on the right are for the calibration period starting at the 27.5.08.*

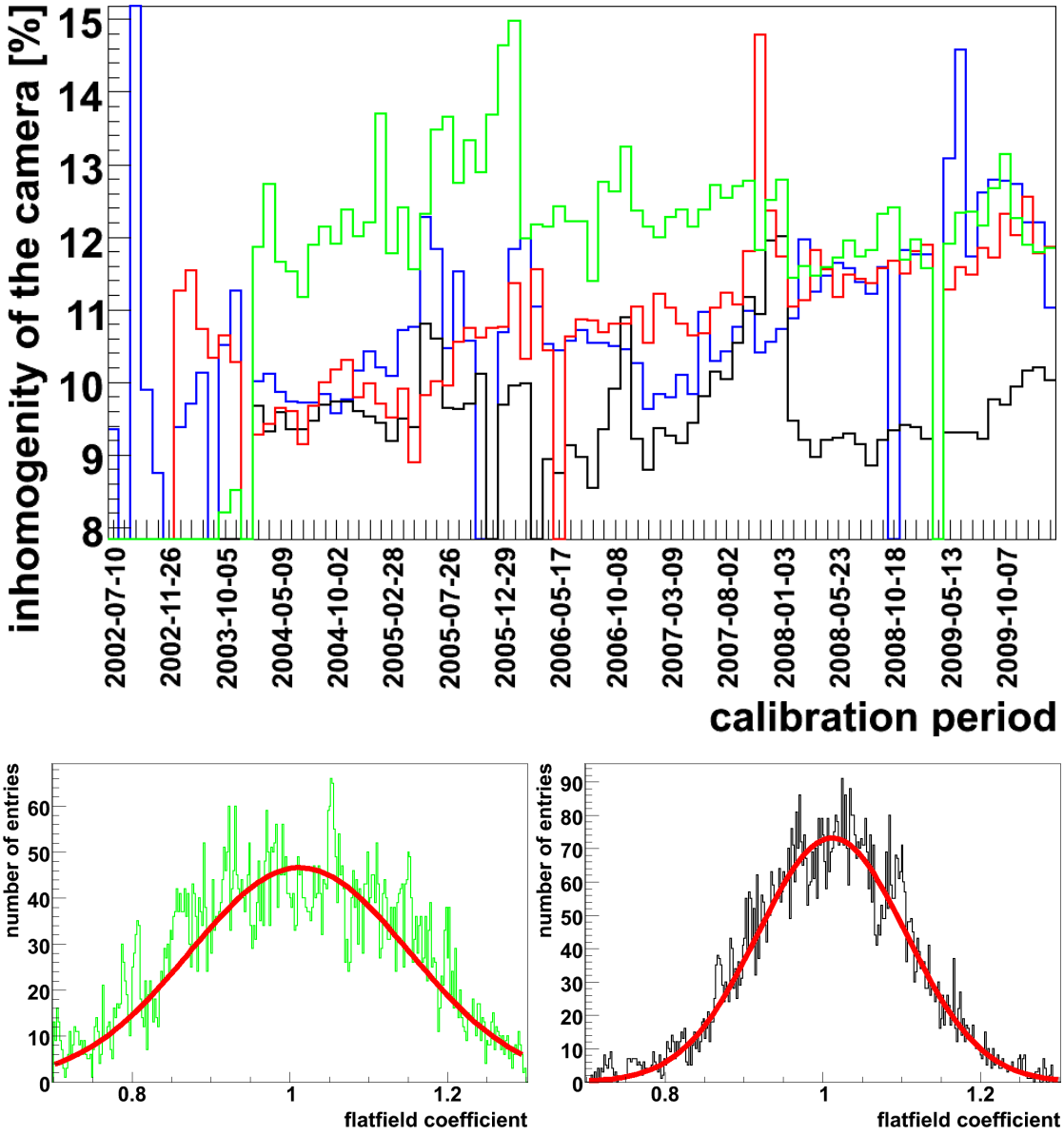

Figure 4.17: *The evolution of the camera inhomogeneity over the whole lifetime of the H.E.S.S. experiment is shown in the upper row. CT1 is drawn in black, CT2 in red, CT3 in blue and CT4 in green. In the lower row two distributions of the γ^{FF} coefficients for the calibration period starting at the 29.12.05 are plotted. The left plot shows the distribution for CT3 and the corresponding Gaussian fit. It is clearly visible that the distribution is wider than the distribution for CT1, plotted on the right. This indicates a problem during the determination of the flatfield coefficients.*

5 Systematic studies of pedestal estimation methods

For a correct conversion of the raw data of a given gain channel of a photomultiplier into an intensity in p.e., the baseline of this channel has to be monitored closely. It depends, for example, on variations of the temperature of the photomultipliers and on problems with the camera electronics. The standard pedestal estimation methods, currently in use by the H.E.S.S. calibration software and their limitations, will be presented below. Furthermore, an improved method will be presented and its capability to cope with the problems of the standard techniques will be discussed.

Dataset

A set of 54 Crab Nebula observation runs, with a lifetime of 22.5 h, as well as the 3 observation runs of the flare of PKS 2155−304 [21], with a lifetime of 1.3 h, were used for the systematic studies of the pedestal estimation methods. All runs were taken with four telescopes and fulfill the standard run selection criteria [14]. If not stated otherwise, the analysis was performed using HAP, a Hillas analysis, with standard cuts. These cuts are based on Hillas parameters. The significance of the detection of a source, i.e. the signal to noise ratio, was calculated using the formula from Li & Ma [22]. The background was estimated using the reflected background method, an illustration is seen in Figure 6.2, for the significance calculations and the extraction of the spectra and the fluxes [14].

5.1 Pedestal estimation methods used in the DST production

At the moment, two different calibration chains are used by the H.E.S.S. collaboration. Their names are derived from their points of origin and are the Heidelberg and the Paris calibration. For the high level analysis of the data, the raw data isn't used directly, instead so called DST files are processed. These files only contain the calibrated intensities after a tail cut. Moreover, some additional loose cuts have been applied, i.e. an event selection based on certain parameters. Because of that, DSTs are significantly smaller and can be processed faster. A similarity of both calibrations is, that the whole raw data file has to be processed once to calculate the pedestal values and a second time to do further calibrations. This excludes these two pedestal estimation methods from the use in the online analysis, as explained in detail in Chapter 6. The main difference between the Heidelberg and the Paris calibration are the different pedestal estimation methods, used to calculate the baselines of the pixels. The exact implementations will be shown below.

5.1.1 Average pedestal estimation

The Heidelberg calibration chain uses a rather simple approach to determine the pedestal position of every gain channel of every pixel for all four cameras. The average number of pixels, which contain a Cherenkov signal, is $\mathcal{O}(10)$. The rest of the pixels in the camera can be used for the pedestal calculation. As a first step, every pixel contaminated by Cherenkov light has to be excluded. To decide, whether a pixel should be used or not, both gain channels of the pixel itself and its direct neighbors are checked, if they exceed a given threshold. Is this true for more than one pixel, it is not used. The next step is the calculation of the mean over 5000 consecutive events, excluding those with a Cherenkov signal. The mean of this distribution is then used as a baseline for the pixel for these 5000 events. This corresponds to $\approx$30 s of run time. In Figure 5.1 the time evolution of a typical Heidelberg pedestal position on a scale of a few minutes is shown.

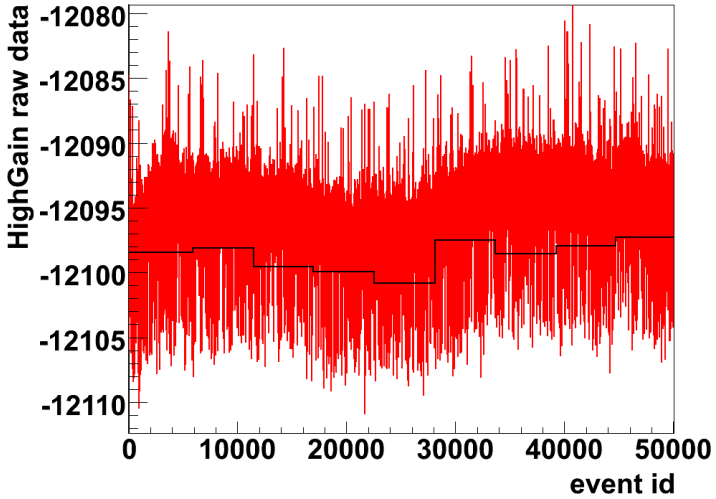

Figure 5.1: *Shown is the HighGain pedestal position in ADC counts of a single pixel for the Heidelberg (black line) and the Paris (red line) pedestal estimation methods as a function of the event id on a time scale of a few minutes. The time gradient of the Paris pedestals can't be seen, because the time between two consecutive event ids is not constant.*

5.1.2 Average pedestal estimation with a time gradient

A different approach for the calculation of the baseline is taken by the Paris calibration. The idea is, that the pedestal value of a pixel is not described properly, if just an average over a given number of consecutive events is used. Instead, a straight line is fitted to the baseline development. It can be described through its starting point and its gradient. This will now be explained in detail. As a first step, the distribution of the intensities around a pixel is calculated. For this, the pixel itself, its first, second and third neighbors are used. Then pixels with intensities, which are too high offset from the mean of this distribution, are excluded. After that, events with too many pixels with a signal are rejected from the pedestal calculation. If the event survives, pixel which are surrounded by Cherenkov light contaminated pixels aren't used either. The intensity of a pixel is used to calculate the pedestal position, if the pixel has no neighbor pixels, which exceed a given threshold. The intensity is then filled into a histogram, which describes the time evolution of the pedestal position of the pixel. Finally, the histogram is divided into intervals and the time evolution

in those intervals is estimated by a straight line. The starting point of the pedestal position in the interval and the time gradient are all that is necessary to describe the evolution of the baseline of the pixel. The result is shown in Figure 5.1. The average number of pedestal points calculated for a run are in $\mathcal{O}(10)$.

5.1.3 Comparison of Hillas parameter distributions

To verify the compatibility of both calibration chains the Hillas parameters of the air showers have been compared. Figure 5.2 shows the distribution of the reconstructed *mean reduced scaled width* and *mean reduced scaled length* for a typical observation run on the Crab Nebula. As expected, the two match and the shape of the shower is not reconstructed differently. The *image amplitude* of the shower, which is important for the energy reconstruction of the primary particle is compatible as well, as shown in the lower part of Figure 5.2.

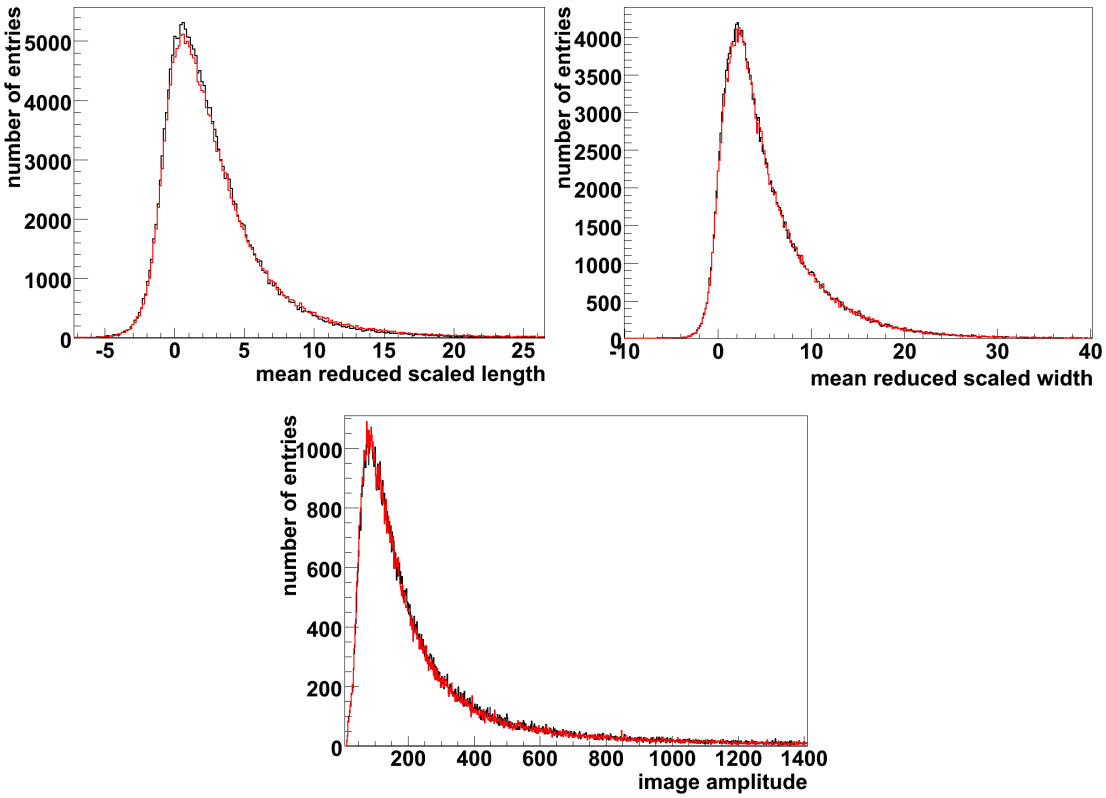

Figure 5.2: *The distribution of the mean reduced scaled length for a typical Crab observation run is shown on the upper left side, the mean reduced scaled width on the upper right side. Below the image amplitude for one camera is plotted. The Heidelberg calibration is in black and the Paris calibration is in red. The comparability of the Paris and Heidelberg calibration is obvious.*

Problems with the pointing model of the Heidelberg calibration

During the comparison of the Paris and Heidelberg calibrations, a rotation of the *center of gravity* distributions of several cameras was found for some calibration periods. An example is shown in Figure 5.3. It is obvious, that the distribution for CT1 is rotated by $\approx 10°$. The reason is an abnormal high pointing correction. It should normally compensate the

influence of the distortion of the telescope structure, but in this case leads to an unjustified big correction. The problem was under investigation in Heidelberg and it turned out, that an incorrect transformation of negative rotation angles was the source.

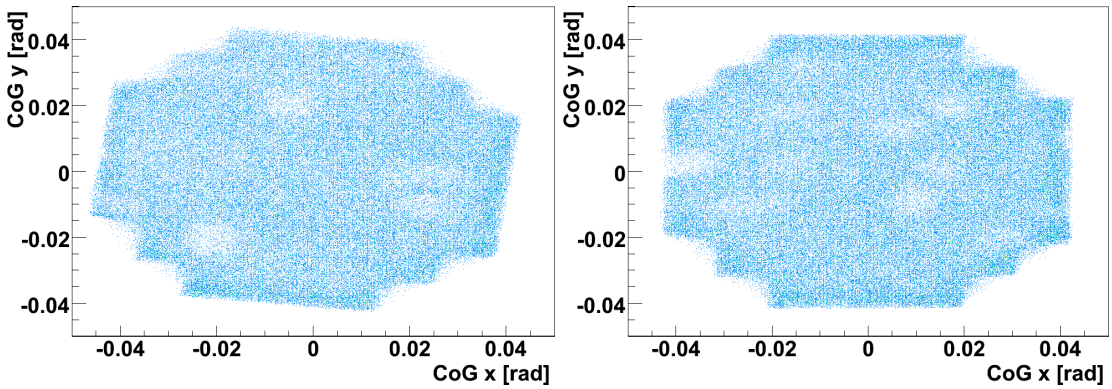

Figure 5.3: *Center of gravity distribution for CT1 on the left and CT2 on the right for the Crab observation run 43490. The rotation of CT1 by* $\approx 10°$ *is due to problems with the pointing model.*

5.2 Improved pedestal estimation method

With the implementation of the online analysis, see Chapter 6, a third pedestal estimation method was introduced into the H.E.S.S. software. The concept of a running average, used by the online analysis, was taken as the basis of the improved pedestal estimation method. This method was developed in the course of this thesis and is the main focus of this work. Contrary to the other methods, no knowledge of the neighboring pixels is needed. In addition, no information about future events is necessary. An exception is the correction of the baseline oscillations, which needs to calculate averages over several pixels, see Subsection 5.2.2. The improved pedestal estimation method calculates new pedestal values using the following formula for a running average:

$$Mean^{HG}_{New} = F \cdot Mean^{HG}_{Old} + (1 - F) \cdot ADC^{HG} \tag{5.1}$$

$$Mean^{LG}_{New} = F \cdot Mean^{LG}_{Old} + (1 - F) \cdot ADC^{LG} \tag{5.2}$$

With:

- HG, LG being the HighGain or LowGain channel of a pixel.
- $Mean_{New}$ the new pedestal value of the given channel.
- $Mean_{Old}$ the old pedestal value of the given channel.
- ADC the intensity of the given channel in ADC counts.
- F being the weighting factor between the new event and the old pedestal position. Meaning a higher weight of new events for lower values of F.

The proper value of F will be explained in Subsection 5.2.1. In addition, the square mean pedestal value $SquareMean$ for both channels of a pixel is stored. New values are calculated using a similar equation:

$$SquareMean^{HG}_{New} = F \cdot SquareMean^{HG}_{Old} + (1 - F) \cdot \left(ADC^{HG}\right)^2 \tag{5.3}$$

$$SquareMean^{LG}_{New} = F \cdot SquareMean^{LG}_{Old} + (1 - F) \cdot \left(ADC^{LG}\right)^2 \tag{5.4}$$

With the mean and the square mean pedestal value, the deviation of the pedestal distribution $Deviation$ can be calculated:

$$Deviation^{HG}_{New} = \sqrt{SquareMean^{HG}_{New} - \left(Mean^{HG}_{New}\right)^2} \tag{5.5}$$

$$Deviation^{LG}_{New} = \sqrt{SquareMean^{LG}_{New} - \left(Mean^{LG}_{New}\right)^2} \tag{5.6}$$

The deviation of the pedestal distribution is used to exclude pixels contaminated by Cherenkov light from the pedestal calculations. To do this, the pedestal subtracted ADC value of a given gain channel, called corrected HighGain/LowGain value, is checked, if it exceeds a given threshold. This is described through the following inequality:

$$ADC^{HG} - Mean^{HG} \leq T \cdot Deviation^{HG} \tag{5.7}$$

$$ADC^{LG} - Mean^{LG} \leq T \cdot Deviation^{LG} \tag{5.8}$$

If it is true, the pixel isn't contaminated by Cherenkov light in the given channel. The higher the value of T, the higher the probability, that the event is used to calculate a new pedestal position for the given pixel. The correct value of the threshold factor T and the weighting factor F has to be determined, as shown in Subsection 5.2.1. A problem with this method is, that pixel with a rapid baseline drift could be flagged as containing Cherenkov light for the remainder of the run. To correct for this, the number of consecutive Cherenkov events is stored for the two gain channels of every pixel. If it should exceed a certain limit, called *HighNumEvents* (*HNE*), a pedestal recalculation is forced. The correct value for *HNE* is also explained in Subsection 5.2.1.

5.2.1 Determination of the improved pedestal estimation method's parameters

To calculate a reasonable baseline estimation for every PMT, the correct value for each parameter of the running average pedestal estimation method has to be determined. This is done for the weighting factor F as a first step. The change in the development of the baseline of a single pixel, for different values of the weighting factor F, is shown in Figure 5.4 for a flatfield run. The rapid change of the pedestal position is easy to see. A weighting factor F of 0.8 seems to produce the best results.
Different pedestal distributions have been checked to get a more detailed overview of the influence of the weighting factor F. Figure 5.5 shows the change of the HighGain deviation distribution, and the change of the HighGain to LowGain ratio projection, for a whole camera for different values of the weighting factor F.
With a low weighting factor F, the distribution of the deviation of the pedestal positions is getting narrower and it is shifted to a peak around zero. However, at the same time

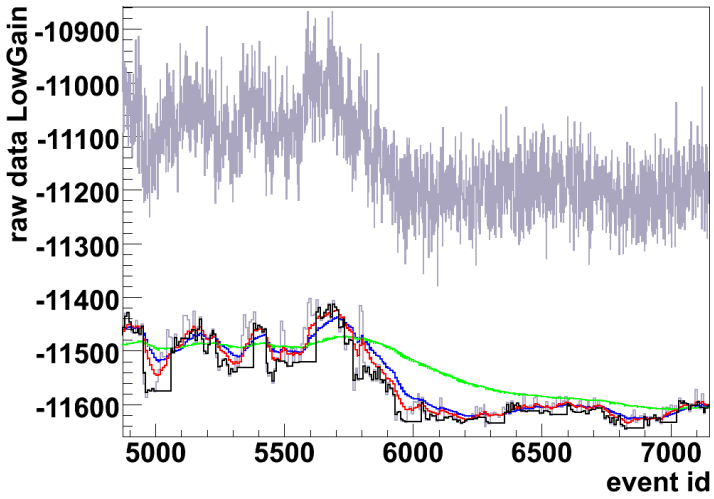

Figure 5.4: *Shown above is the development of the baseline in ADC counts of a single pixel for a flatfield run. The raw data distribution, consisting of signal and background events, is drawn in gray. The pedestal values of the improved pedestal estimation method are shown for different values of the weighting factor F; 0.2 in black, 0.8 in red, 0.9 in blue and 0.98 in green. A weighting factor F of 0.8 provides the best results. Forced pedestal recalculations are visible for a weighting factor F of 0.2.*

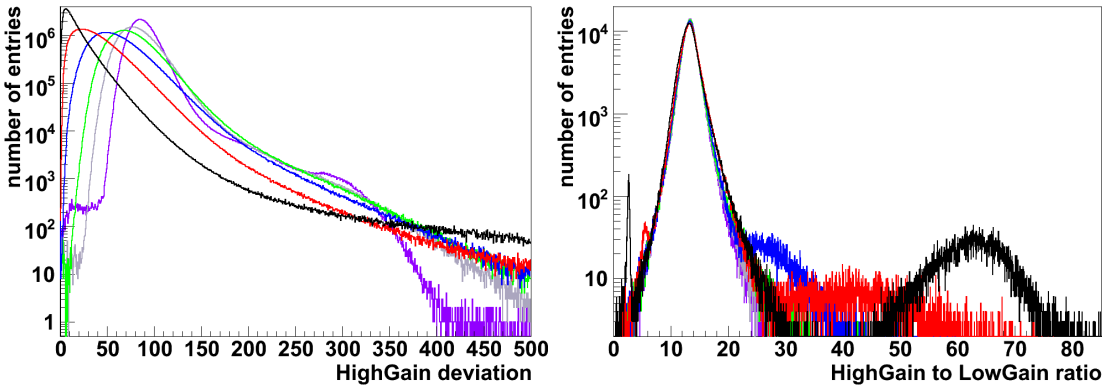

Figure 5.5: *Shown above on the left side is the projection of the HighGain deviation in ADC counts for a complete camera. Black corresponds to a weighting factor F of 0.2, red to 0.4, blue to 0.6, green to 0.8, gray to 0.9 and purple to a factor of 0.98. The influence of the different weighting factors F is clearly visible. The stronger the response to a pedestal change, the more the peaks of the distribution are shifted to zero. Additionally, the number of high deviation events increases significantly. The right Figure shows the projection of the HighGain to LowGain ratio, using the same color coding. For low values of F, the distributions gets distorted. Broken pixels are excluded in all projections.*

the number of high deviation events increases significantly. The reason is, that with smaller values for F, more and more pixels are used to calculate the baseline, which are contaminated with Cherenkov light. The leads to the base line being almost always at the same level as the pixel's intensity. As a result, the number of reconstructed gamma events is significantly reduced for lower values of F, as seen in Figure 5.6. As a compromise between a fast response to shifts in the baseline and not using pixels contaminated by Cherenkov light, the weighting factor F is set to a value of 0.8. This corresponds to the usage of 20 % of the value of a new pedestal event and 80 % of the old value, see equation 5.1.

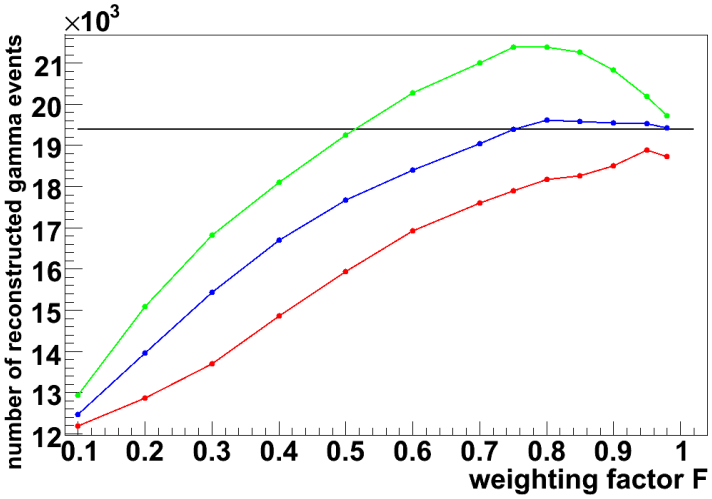

Figure 5.6: *The number of reconstructed gamma events as a function of the weighting factor F for three different values of the threshold factor T is shown. The red line corresponds to a value of 3, the blue to 4 and the green to 5. The black line is the number of reconstructed gamma events, if the Heidelberg pedestal values are used. A sample of 54 observation runs, with the Crab Nebula as target, were used to generate this plot.*

As a next step, the correct value of the threshold factor T has to be determined. It is responsible for the exclusion of pixels, which are contaminated with Cherenkov light, see equation 5.7. If the parameter is set too low, all pixels will be rejected from pedestal calculations. If it is set too high, the baseline will be shifted upwards, because Cherenkov events are used to estimate the pedestal value. As a result, the number of reconstructed gamma events is lower, because less pixel survive the tail cut and the shape of the Hillas ellipses are distorted. This is also visible in Figure 5.6. Although the number of events is higher for a threshold factor T of 5, the significance of the detection of the Crab Nebula is getting lower. This can be seen in Figure 5.16. Another way to see the influence of the parameter T is to plot the projection of the corrected LowGain for a camera and the deviation of the LowGain baseline. This is visible in Figure 5.7. For lower threshold factors T, the deviation of the LowGain is getting smaller. However, for a value of 1, too few pixels are used to calculate the pedestal position, thus increasing the deviation. The threshold factor T is set to 4 for the improved pedestal estimation method. This is done to obtain a small enough deviation of the corrected gain distributions on the one hand, and a high enough number of reconstructed gamma events on the other hand.
As mentioned in Section 5.2, a rapid shift in the baseline of a gain channel could lead to the exclusion of the channel from the pedestal calculation for the remainder of the run. To prevent this, *HNE* is set to 7 for the improved pedestal estimation method. The reason for this is clearly visible in Figure 5.8, which shows the projection of the distribution of consecutive Cherenkov events for a complete camera.
To cross check the running average pedestal estimation, several distributions have been used for a comparison with the other two methods, for instance the corrected gains of a pixel and the ratio of the HighGain and LowGain channel in the linear range of operation of the amplifiers. Figure 5.9 shows the resulting distributions. Here, all the pixel of a camera are used to fill the histograms, except those flagged as broken. As expected, the distributions show the same behavior, but are not equivalent.

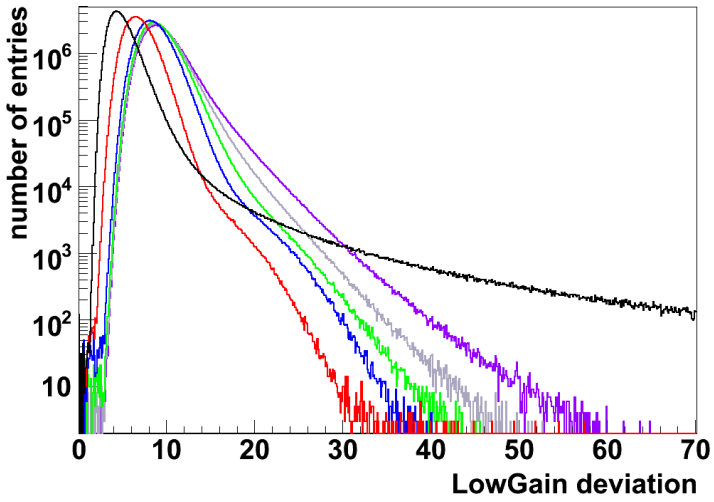

Figure 5.7: *The influence of the threshold factor T on the projection of the deviation of the LowGain in ADC counts is shown for a complete camera. Black corresponds to a value of 1, red to 2, blue to 3, green to 4, gray to 5 and purple to 6. For lower threshold factors T, the deviation of the LowGain is getting smaller. However, for a value of 1 an insufficient number of pixels is used to calculate the pedestal position, thus increasing the deviation.*

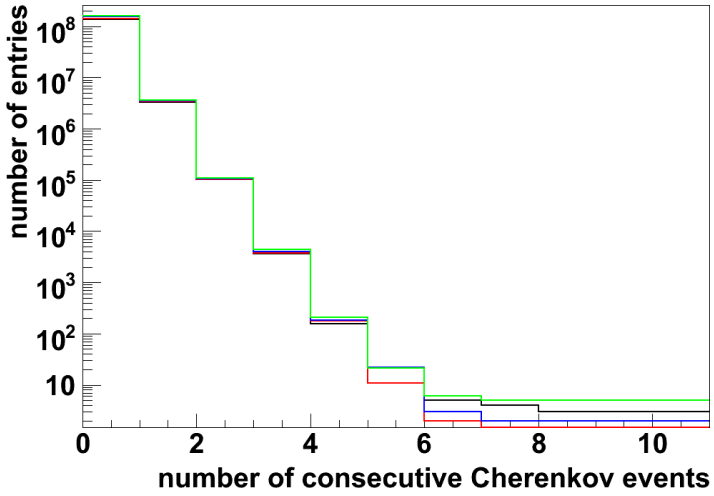

Figure 5.8: *Plotted is the number of consecutive signal events for all four cameras for a Crab Nebula observation run. The HNE parameter is set to 7, not to force unnecessary pedestal recalculations. CT1 is the black, CT2 the red, CT3 the blue and CT4 the green line.*

A disadvantage of the running average pedestal estimation method is, that at the beginning of the run approximately the first 100 events can't be used. This is because several events have to be processed for a correct determination of the baseline. This can be solved by calculating a start pedestal mean and square mean value for every gain channel of every pixel, using the first 200 events of a run. With this, all events of a run can be processed normally. Nonetheless, this is not possible for an on the fly pedestal calculation, because the knowledge of future events is required. In this case, the ADC values of the first non Cherenkov event, for a given pixel, are used as the start pedestal position with a deviation of zero.

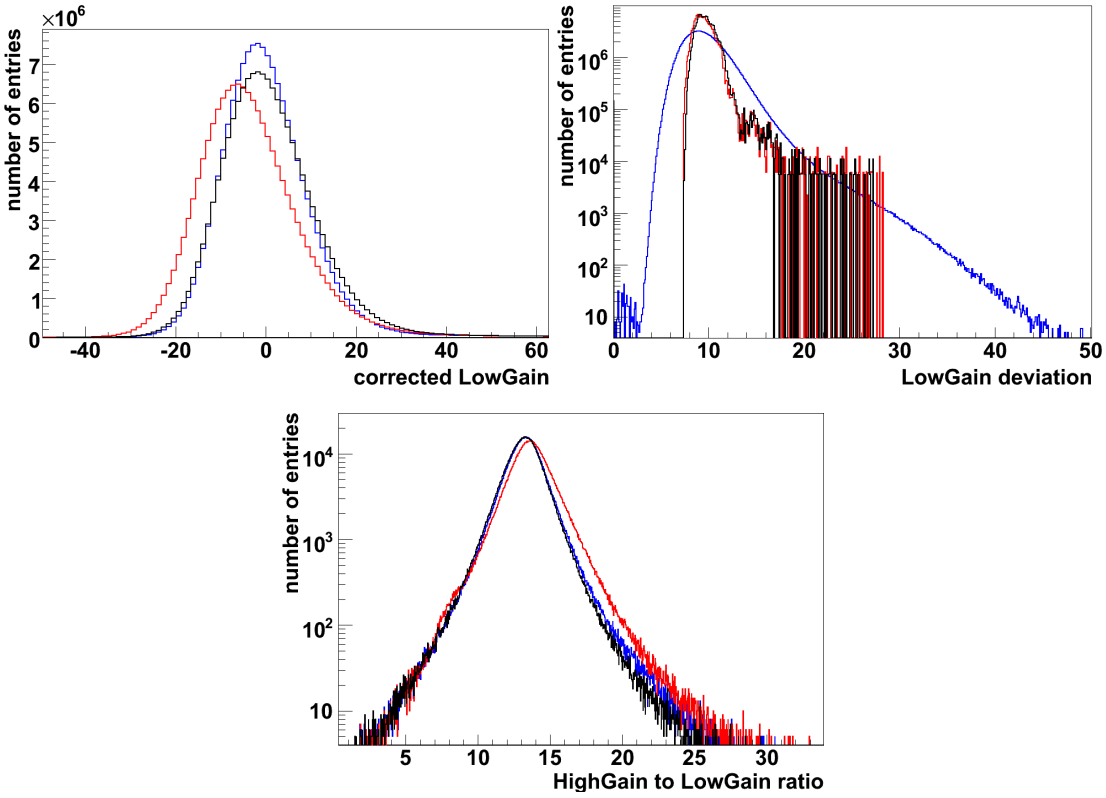

Figure 5.9: *Comparison of the three different pedestal estimation method. In the upper left, the projection of the corrected LowGain in ADC counts for a camera is shown, in the upper right, the corresponding LowGain deviation in ADC counts. The bottom plot is the distribution of the HighGain to LowGain ratio. Broken pixel were excluded. The Heidelberg distribution is in black, the Paris one is in red and the running average one is in blue. The binning effects in the upper right plot are due to the Paris and Heidelberg calibration using a mean deviation value for a given number of consecutive events and thus reducing the amount of different deviation values.*

5.2.2 Correction of baseline oscillations

A known hardware problem of the cameras are the so called baseline oscillations. They occur, if the cameras are read out twice or more in a time interval smaller than 2 ms. The effect is a shift of the baseline of one half of the pixels of a camera. The source is a fluctuation of the power supply. It is only a small shift of about 10 ADC counts. Because of that, it can only be detected by averaging over the corrected gain values of all pixels of a half of a camera. Furthermore, pixels contaminated with Cherenkov light have to be excluded. Additionally, the effect is not visible, if an average over the complete camera is calculated. Figure 5.10 shows the baseline oscillation of a single half of the camera for both gain channels as a function of the time interval between the last two events. A clear sinusoidal curve is seen.
The baseline oscillation of one amplification channel should be correlated with an oscillation of the other channel for the same half of a camera. The reason is, that the same power supply is used for both channels of one half of a camera. This is visible in Figure 5.10 as well, because the shape of the oscillation in the LowGain matches the one seen in the HighGain. The only difference is a bigger spread of the distribution in the HighGain. This is easily explained by the bigger amplification of little deviations. A correlation can also be seen in

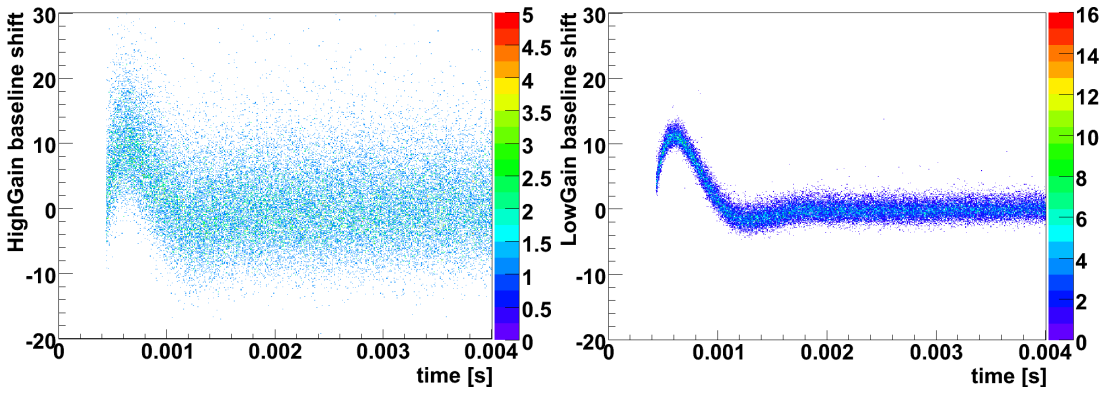

Figure 5.10: *The left side shows the baseline oscillation of the HighGain channel in ADC counts as a function of the time between the last two events. On the right side, the same distribution for the LowGain channel is seen. Both channels show the same behavior for the baseline oscillations. Only the spread of the distribution is significantly bigger in the HighGain.*

Figure 5.11. Here, the baseline oscillation of the LowGain channel is shown as the function of the oscillation of the HighGain channel for one camera side. Because of the correlation, only the LowGain channel is used to determine the baseline oscillations in the improved pedestal estimation method. See below for further details.
In addition, the correlation between the oscillation of the two camera sides has been checked and a dependency between both was detected, see Figure 5.11. This correlation, however, is not used in the baseline oscillation correction.

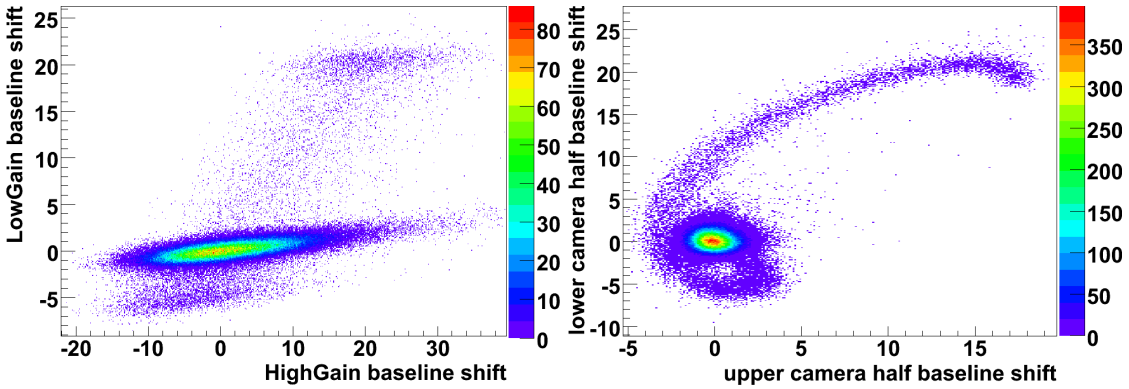

Figure 5.11: *The correlation of the HighGain and LowGain baseline oscillations in ADC counts for one half of a camera is shown on the left. As expected, the baseline oscillations in both gain channels are linear. The bigger spread of the distribution in the HighGain is due to a higher amplification. The LowGain baseline oscillation in ADC counts for the lower half of the camera as a function of the LowGain baseline oscillations in ADC counts of the upper half of the camera is plotted on the right. A clear correlation of the baseline oscillations of the two sides is visible. Nonetheless, this correlation is not used in the correction of the baseline oscillations.*

The improved pedestal estimation method uses the fact, that the baseline oscillations occur only in a specific time window after an event has been read out. Because of that, the camera is only checked for an oscillation, if the time interval between the current and the last event is less than 2 ms, see Figure 5.10. If an event falls into this category, the mean of the corrected

LowGain for the two camera sides is calculated. Pixels which were rejected for pedestal calculation by equation 5.7 are excluded. This mean is then added to the baseline of all pixels of the corresponding half of the camera for both gain channels. The internally stored mean and square mean pedestal values are calculated normally. This is justified, because, with a maximal shift of about 20 ADC counts and a weighting factor F of 0.8, a negligible increase of 4 ADC counts of the baseline of the pixels occurs. However, there is a drawback to the time window mentioned above. Namely, that a possible baseline oscillation can't be corrected, if the time between two events couldn't be determined. Nonetheless, the number of such events should not exceed $\mathcal{O}(10)$ per run. This is negligible in comparison to the number of events, which are outside of the time window. They are in the order of 100000 events and this does not rectify a correction of those.
The Paris calibration also corrects for baseline oscillations, using a slightly different method. At first, the pixel, it's neighbors and next neighbors are checked, whether they are contaminated by Cherenkov light. If too much of these pixels are contaminated, the pixel itself is not used for the averaging over the half of a camera. If more than 100 pixel are found experiencing a shift, the mean of the LowGain half of the camera is calculated. Then the baseline oscillation is corrected with that value in both channels. Another difference to the method mentioned above is, that every event is checked for baseline oscillations.
At the moment of the writing of this thesis, a baseline oscillation correction is implemented in the Heidelberg analysis. Due to lack of time, this method could not be tested and isn't used in this thesis.
To check if the baseline oscillation corrections work, the half of the camera mean distributions of the corrected gain values for a whole run, excluding Cherenkov pixel, have been calculated. This was done for pedestal values calculated by the Heidelberg calibration, the Paris calibration and the running average pedestal estimation method. As mentioned above, no correction for oscillations is expected from the Heidelberg calibration. The results can be seen in Figure 5.12. If the baseline oscillations are corrected, a Gaussian like distribution around zero is expected. This can be seen for the distributions of the improved pedestal estimation method and for the distributions of the Paris calibration. If no correction is applied, an additional Gaussian peak with a shifted mean is expected, which is shown by the Heidelberg calibration.

5.2.3 Improvement over other methods

The main advantage of the running average pedestal estimation is the possibility of an on the fly pedestal calculation. A necessity, for example, in the online analysis, see Chapter 6. This is possible, because no information about future events is needed to calculate the current baseline. A drawback of the improved method is, that no small pedestal files can be created. They would contain all the necessary information to describe the baseline evolution for the complete run for both channels of every pixel. The files of the Heidelberg and Paris calibration are $\mathcal{O}(10\,\mathrm{MB})$ big. They can be used, if any recalibration of the run should be necessary, which does not require a pedestal recalculation. The file size for the running average pedestal method would be in the order of several GB, because of that no pedestal files are created. Though, the time loss, due to a recalculation of the pedestal position with every recalibration, is negligible, because this is not done often.
Another advantage is the successful correction of the baseline oscillations of the cameras, which was demonstrated in Subsection 5.2.2. Moreover, the Paris and Heidelberg correction suffer from a drawback compared to the improved method. Namely, the correction of possible

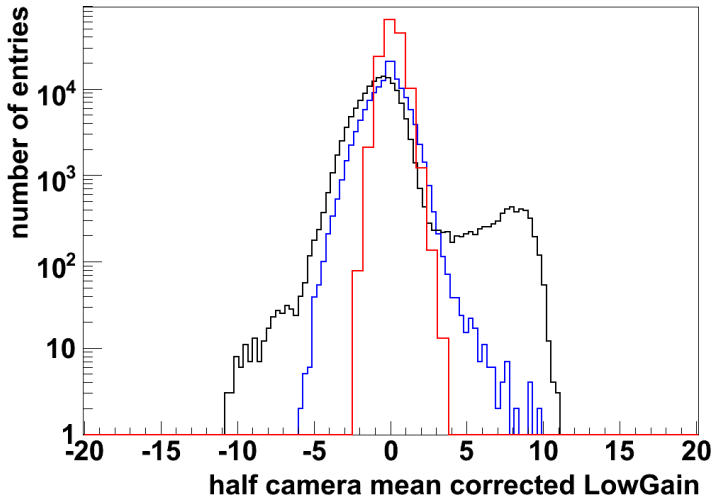

Figure 5.12: *In this plot the mean of a half of the camera for the corrected LowGain in ADC counts is shown. Pixels contaminated by Cherenkov light are not included. The Heidelberg calibration (black line) does not correct for baseline oscillations. This is clearly visible in the additional peak of the distribution. The Paris calibration (red line) uses a correction for the oscillations, as well as the improved pedestal estimation method (blue line). Both correct the baseline oscillations and a half camera distribution centered around zero is the result.*

baseline oscillations, even if the time between two events is bigger than the time window in which baseline oscillations could occur. Additionally, strong variations of the baseline of a pixel on a small time scale cannot be followed by the standard pedestal estimation methods. This can be seen in the left plot of Figure 5.13, where a time evolution of the LowGain of pixel 864 of CT3 for the flatfield run 43556 is plotted. It is obvious, that the Heidelberg pedestal values do not describe the real baseline evolution. This is especially true for the corrected LowGain distribution which is shown on the right in Figure 5.13. Expected are two Gaussian peaks, one for the background, and one for the signal. The distribution for the Heidelberg calibration is distorted, whereas the running average pedestals show the desired behavior. Moreover, the correctness of a value of 0.8 for the weighting factor F is visible.
If a jump in the baseline of a pixel occurs, the Heidelberg and Paris pedestal methods are not able to correct for this. This behavior is shown in Figure 5.14, where the time evolution of the pedestal position for a single pixel for both gain channels is plotted. While the running average pedestals have no problem coping with this jump, the Heidelberg and Paris pedestal estimation methods ignore the jump completely. The result is a flagging of the pixel as broken for the complete run in the case of the Heidelberg calibration, whereas the Paris calibration doesn't deactivate the pixel at all.

5.2.4 Influence on the Hillas parameters

The Hillas parameter distributions of different Crab Nebula and PKS 2155−304 observation runs were used as a cross check between the different pedestal estimation methods. In detail, exactly the same calibration and analysis was done, except different pedestal values were used. The resulting Hillas parameter were subtracted from each other and the resulting deviation distributions can be seen in Figure 5.15. There, the difference in the values for the *mean reduced scaled length* and *width* for all the events of a Crab observation runs are shown. The resulting distribution is very small, which indicates a very good match. Additionally,

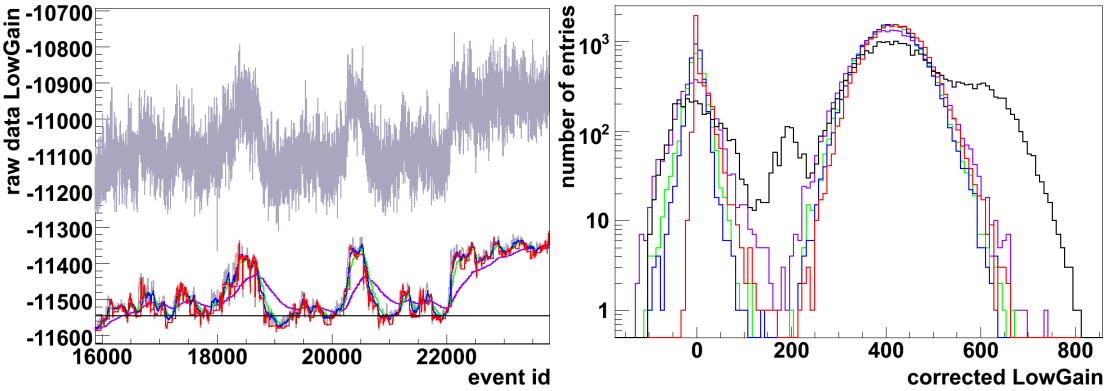

Figure 5.13: *The time evolution of the corrected LowGain in ADC counts of pixel 864 of CT3 for the flatfield run 43556 is shown on the left. The distribution of the raw data is drawn in gray, the Heidelberg pedestals in black. The running average pedestal positions are shown for different values of the weighting factor F; 0.2 is in red, 0.8 in blue, 0.9 in green and 0.98 in purple. It is clearly visible, that the averaging over 5000 events is insufficient to describe the baseline. In the distribution on the right, the corrected LowGain in ADC counts is seen. The improved pedestal estimation method produces the two Gaussian peaks for the background and the signal. The Heidelberg projection is significantly distorted. Furthermore, the value of 0.8 for the weighting factor F is confirmed.*

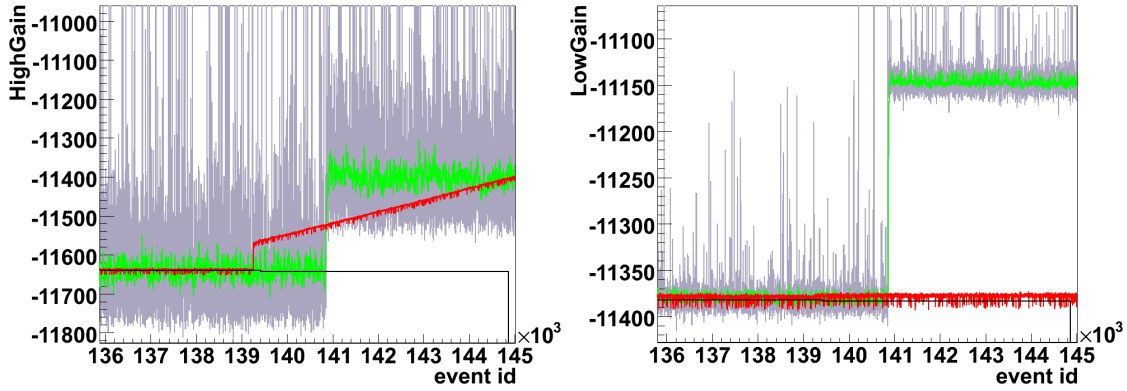

Figure 5.14: *The baseline in ADC counts of a single pixel for both gain channels as a function of the event id is shown. The raw data is plotted in gray, the Heidelberg pedestal values in black, the Paris pedestal values in red and the improved ones in green. A jump in the baseline of the pixel is seen, which is ignored by the Heidelberg calibration. For the Paris calibration, a correction is tried in the HighGain channel, but it is unsuccessful. However, the improved pedestal estimation method has no problems adjusting to the shift. Moreover, the time gradient of the Paris pedestal estimation method is visible in the HighGain channel.*

the *image amplitude* deviations for the four cameras, seen in the lower plot, show the same behavior. The small peaks with a 5 p.e. distance from each other are due to pixel surviving the 5/10 tail cut or being excluded by it.

5.2.5 Influence on the significance

To further check for any significant changes in the behavior of the analysis, introduced through the improved pedestal estimation method, the two data sets of the Crab Nebula

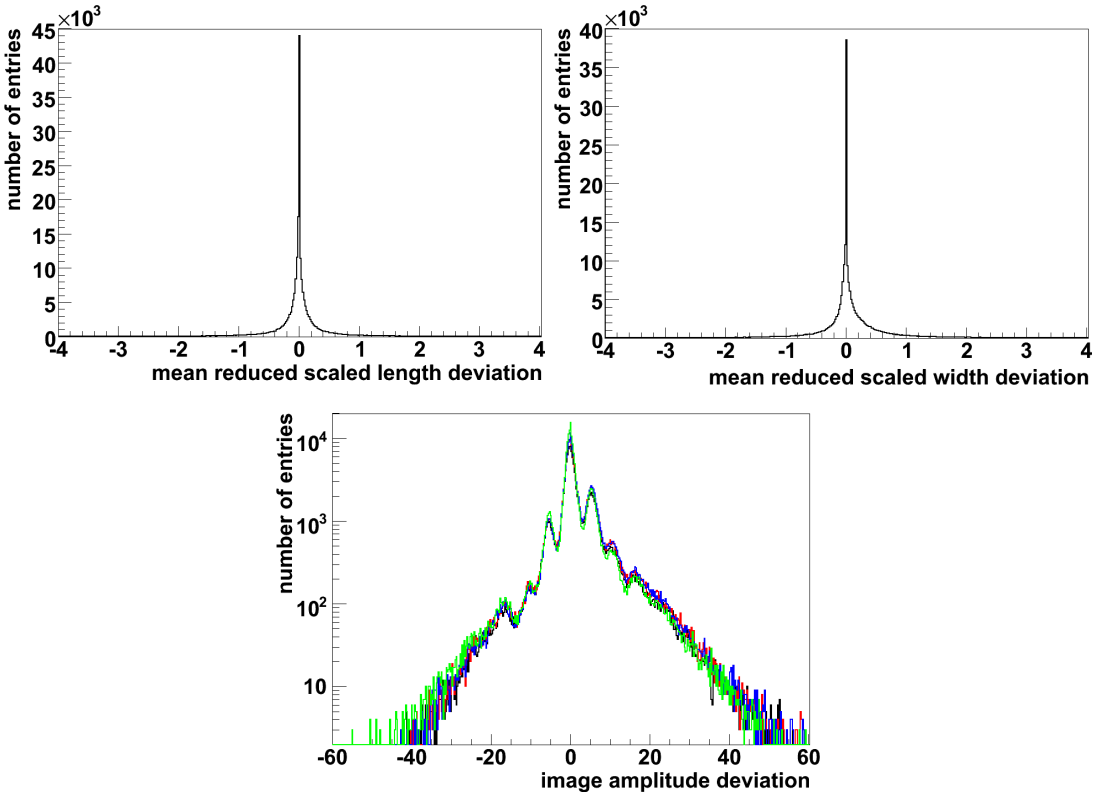

Figure 5.15: *The plots show the deviation between the calculated Hillas parameters using the running average pedestal estimation method and the Heidelberg one. For every event, the difference in the given Hillas parameter is filled in the histograms. The mean reduced scaled length and the mean reduced scaled width deviation distributions are plotted on the upper row in this order. The lower Figure shows the deviation in the image amplitude for all four cameras. CT1 is drawn in black, CT2 in red, CT3 in blue and CT4 in green. As expected, no significant deviations are visible. The small peaks with a* 5 *p.e. distance are due to pixel surviving the 5/10 tail cut or being excluded by it.*

and PKS 2155−304 observation were chosen. The calibration and analysis of the run data was exactly the same, except for the option to choose between two different pedestal estimation methods. The result of this analysis can be seen in Figure 5.16. The significance of the detection of the two sources as a function of the lifetime for the analysis using the Heidelberg pedestal values and the analysis using the running average pedestal estimation method with different threshold factors T can be seen. Only a small deviation is visible, which indicates a compatible behavior of the two.

5.2.6 Influence on the spectrum

At last, the spectra of the 54 observations runs on the Crab Nebula, extracted from the analysis mentioned in Subsection 5.2.5, were checked for differences. In Figure 5.17, the two resulting spectra are plotted. The one using the running average pedestals is in red and the one using Heidelberg ones is in black. The index and the flux are compatible within the range of the error margins.

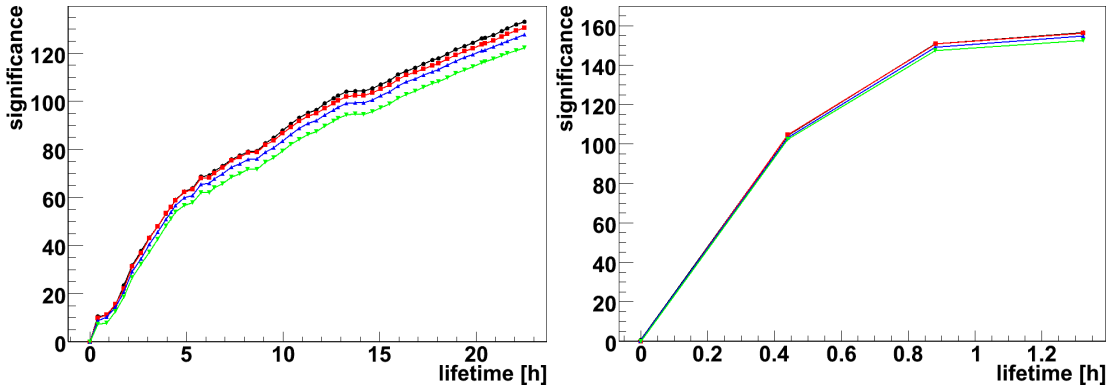

Figure 5.16: *The significance of the detection of the source as a function of the lifetime for a set of 54 Crab Nebula observation runs, calibrated using different pedestal estimation methods and analyzed using HAP, is shown on the left. The black line corresponds to the Heidelberg pedestal values being used, the red line belongs to the running average pedestal values with a threshold factor T of 3, the blue line to a factor of 4 and the green line to a factor 5. On the right, the significance of the detection of the PKS* 2155−304 *flare is shown with the same color coding. It is obvious, that the two pedestal estimation methods produce compatible results.*

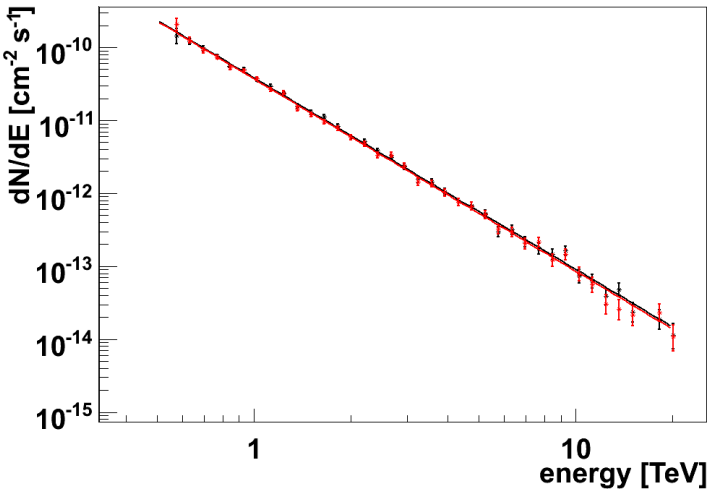

Figure 5.17: *Spectra of the 54 observations of the Crab Nebula extracted out of the analysis performed to generate Figure 5.16. The spectrum belonging to the Heidelberg pedestals is in black and the running average pedestal's spectrum with a weighting factor F of 0.8 and a threshold factor T of 4 is in red. The obtained indexes are* -2.626 ± 0.0025 *for the offline and* -2.637 ± 0.0095 *for the online analysis and the fluxes above* 0.2 *TeV are* $(3.234 \pm 0.0858) \cdot 10^{-10}$ cm^{-2} s^{-1} *and* $(3.157 \pm 0.08639) \cdot 10^{-10}$ cm^{-2} s^{-1} *respectively. They are all compatible within their error margins.*

6 H.E.S.S. online analysis

The online analysis is used to give the shift crew on site in Namibia the possibility to monitor the data, taken by the four telescopes, as it is written to disk. This enables the shift crew to quickly respond to a possible flaring of the observed source, or to detect problems with the data taking, as soon as they occur. Furthermore, a first glance at the significance of the detection and other properties of the observed target are possible [23]. The implementation of the online analysis into the data acquisition (DAQ) and its differences from a standard Hillas analysis will be presented below. In addition to that, a detailed comparison of the abilities of the online analysis with standard Hillas analyses and possible improvements will be discussed.

6.1 Integration into the DAQ

The data acquisition of the H.E.S.S. telescopes has to process and store all the data taken by the four cameras. However, this can not be achieved by a single computer. Therefore, the DAQ divides the data into processable packages and sends these to PCs called nodes. Currently $\mathcal{O}(10)$ nodes are running on the computer farm in Namibia. To integrate the online analysis into the DAQ, a process called *analyzer* is running on every node. It analyzes the raw data that is written to disk by a *receiver* process. On another machine, a process called *analysis server* is running. It is responsible to collect and merge the analyzed data from each node's *analyzer* and to display the results to the shift crew. Figure 6.1 shows an illustration of this integration.

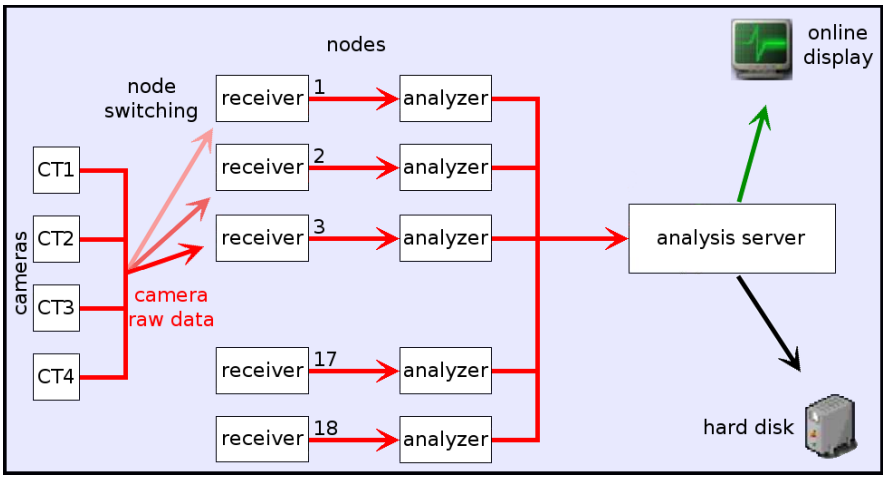

Figure 6.1: *Integration of the online analysis in the H.E.S.S. DAQ. An analyzer process is running on every node listening to the data being processed by the receiver. The analysis server is used to collect the analyzed data and to show it to the shift crew. (Based on a Figure taken from [23])*

6.2 Differences from a standard Hillas analysis

The standard pedestal estimation methods can't be used with the online analysis, because data has to be processed while it is written to hard disk. Therefore, a running average pedestal estimation technique is used, similar to the one described in Chapter 5. Nonetheless, there are several differences:

- The weighting factor F is set 0.98, which corresponds to a weighting of new events of only 2 %.
- The deviation of the pedestal mean is calculated for every 100^{th} pixel, not containing Cherenkov light. However, this was not intended and is due to a bug in the software. Instead, the deviation should be recalculated for every 100^{th} event.
- The maximum number of consecutive Cherenkov events *HNE* is set to 10. If a pixel should exceed this limit, no recalculation is done. Instead, the deviation is increased.
- The start mean pedestal position is set to -12000 ADC counts for both gain channels of a pixel with a deviation of 3000.
- The threshold factor T is set to 4 as well.

Furthermore, no calibration values are available for the conversion of the ADC counts to intensities in p.e. The reason is, that the calibration of the data is done in Europe after the observation period is finished. Because of that, following default calibration values are used:

- The γ_e^{ADC} coefficient is set to 80.
- The HighGain to LowGain ratio is set to $1/0.07143 \approx 14$.
- The flatfield coefficients are all set to 1.

Additionally, a minimum *image amplitude* cut of 80 p.e. is used to reduce the number of events. The H.E.S.S. analysis softwares usually correct for the different influences of the earth's magnetic field. This depends on the target's location in the Northern or Southern Hemisphere. Because most of the sources observed by H.E.S.S. are in a southern direction, the online analysis is tuned for them. The last difference to a normal data calibration is, that no broken pixels are excluded.
The online analysis is based on a standard Hillas analysis, which is called WobbleChain. The H.E.S.S. analysis and calibration softwares are divided into small parts, called makers, which are dedicated to specific tasks. To reject the background of non gamma events, standard Hillas parameter cuts are applied. The H.E.S.S. telescope array uses a so called observation in Wobble mode to avoid systematics in the background estimation [14]. There, the telescopes do not point directly onto a target, instead an offset of 0.5° is used most of the times. The seven background maker of the WobbleChain analysis takes advantage of this and is used in the online analysis as well. A circular shaped region around the source position, called on region, is defined. It has a radius equal to a maximum theta square value of $0.2\,\text{deg}^2$. Moreover, seven so called off regions are placed on a circle around the observation position. Their shape and size are the same as the one of the on region. The radius of the circle around the observation position is equal to the offset used for the observation in Wobble mode. This

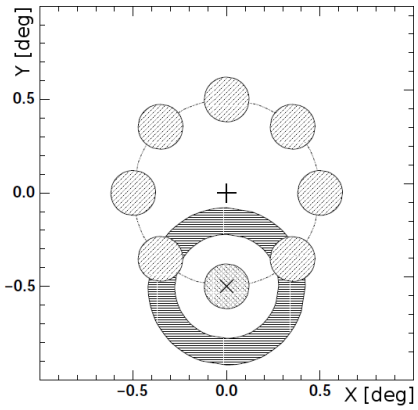

Figure 6.2: *An illustration of the placement of the different regions used for the background estimation is shown for the ring, reflected and seven region background maker. The observation position is marked with a black cross and the source position is marked with a black x. The circular region around the source position is called on region. The reflected and the seven region background maker use the circular shaped regions, placed on a ring around the observation position, as off regions. The seven region background maker always uses seven regions, whereas the reflected background maker can use any number of off regions bigger than 1. The ring background maker uses a ring-shaped off region placed around the source position. (Figure taken from [14])*

is illustrated in Figure 6.2. The number of gamma events in the on region and the off regions are then used to calculate the significance of the detection of the source. For this the formula from Li & Ma [22] is used.
In addition, a theta square plot is filled. It shows the number of gamma events as a function of the radial distance to the target position. The excess sky map is produced using an online analysis background maker. It fills histograms with the coordinates of the direction of the incident gamma-ray and subtracts the background. These plots are displayed on monitors in the control room and a screen shot can be seen in Figure 6.3. Furthermore, the corrected HighGain camera distribution for every telescope is shown.

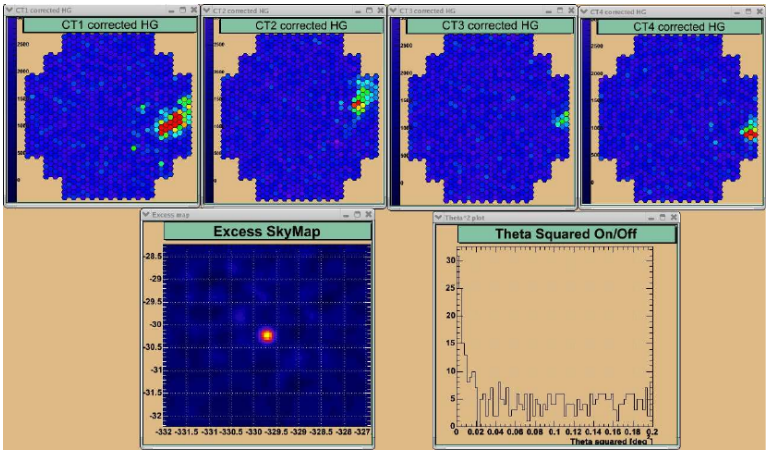

Figure 6.3: *Screen shot of the online analysis display, which shows the corrected HighGain distribution for all four telescopes in the upper row. An excess sky map of the direction of the gamma showers is visible in the lower row, as well as a theta square plot of the radial distance of the shower directions to the target position. (Figure taken from [23])*

6.3 Comparisons of the online and the offline analyses

To check the validity of the results, which the online analysis produces, a step by step comparison of the online data with the offline data will be presented. Expected are comparable significances and spectra for point-like sources, because the online analysis was designed with those in mind. However, for extended sources the fixed size and position of the off regions will most likely result in a overlap of the background regions with the source region. Therefore, the background is contaminated with signal events and the signal to noise ratio should be very low. The distribution of the pedestal values and the Hillas parameter on the other side, should be comparable.

Dataset

A set of 54 Crab Nebula observation runs with a lifetime of 22.5 h, as well as as a set of 99 observation runs of RX J1713.7−3946 with a lifetime of 42.8 h were used for the comparison of the online analysis with the offline analyses. All runs were taken with four telescopes and fulfill the standard run selection criteria [14]. If not stated otherwise, the analyses were performed using HAP and the WobbleChain with standard cuts. These are based on Hillas parameters. The significance of the detection of the sources was extracted using the reflected background maker for HAP and the seven background maker for the WobbleChain [14]. The excess sky maps were created using the online analysis background maker and the ring background maker. The spectra and the fluxes were obtained using HAP with the reflected background maker [14]. An illustration of the different background estimation methods is seen in Figure 6.2.

6.3.1 Pedestal distributions

As stated in Section 6.2, the online analysis uses a running average pedestal estimation method. It is similar to the improved pedestal estimation method described in Section 5.2. It was shown, that the resulting pedestal distributions are compatible. This should also apply for the baselines, used by the online analysis. Due to the implementation of the online analysis, several characteristics can be predicted. For example, the pedestal start values are set to fixed values. This includes an extremely high deviation, which is only updated every 100^{th} pixel. An increased number of events with high offsets of the estimated baseline to the real one should be the result. Furthermore, the splitting of the data onto several nodes results in a multiplication of the behavior described before, by a factor equal to the number of nodes. To simulate this, 18 nodes, the current amount of nodes in Namibia used for observation runs, has been assumed for this comparison. The confirmation of this predictions is shown in Figure 6.4. The distributions of the projection of the corrected LowGain pedestal values match. However, the influence of the wrong start values can be seen, as well as the simulated influence of the splitting of the analysis on several nodes. As expected, the distribution of the deviation is significantly wider for the online analysis. In addition, the HighGain to LowGain ratio match.

6.3.2 Hillas distributions

To check for possible influences on the Hillas parameter distributions several different observation runs have been compared. This will be presented in three steps. At first the influence

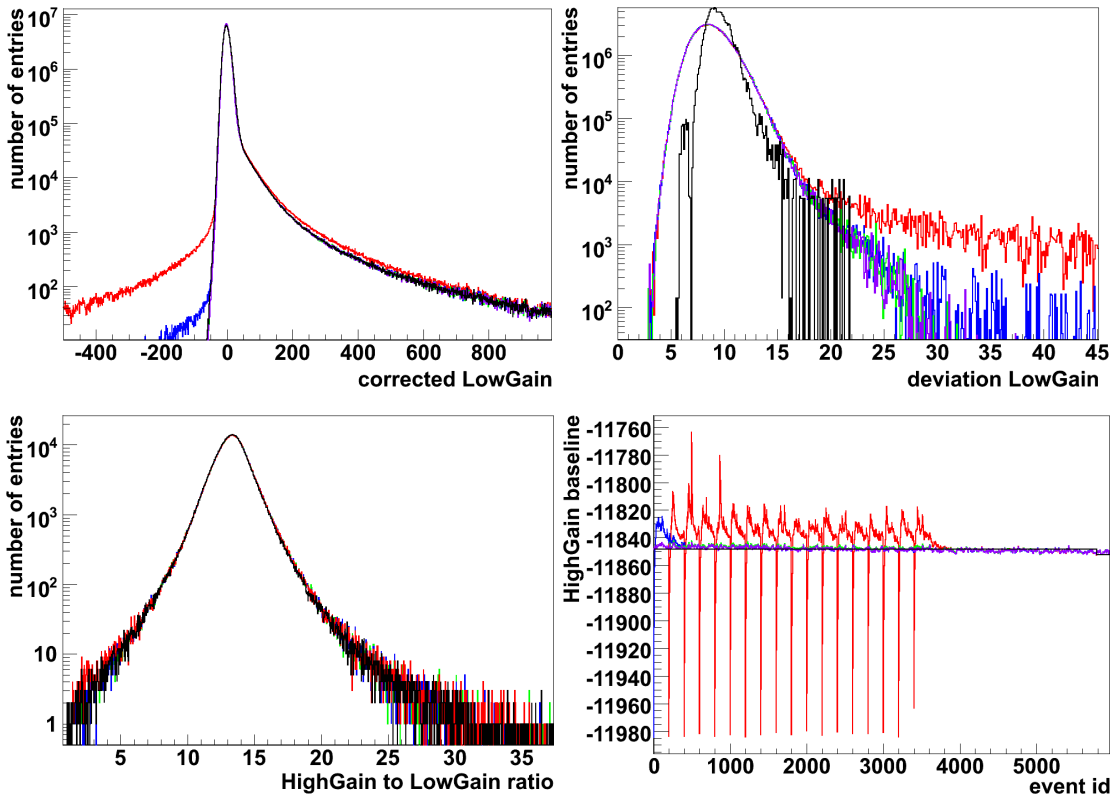

Figure 6.4: *Shown are the projection of the corrected LowGain distribution in ADC counts of one camera for a complete Crab Nebula observation run, as well as the deviation of the LowGain in ADC counts in the upper row. The HighGain to LowGain ratio distribution and the development of the mean baseline of a whole camera for the HighGain channel in ADC counts for the first 6000 events is plotted in the lower row. The Heidelberg pedestal values are drawn in black and the online analysis ones in red. The result, if no splitting of the data on the nodes is simulated, is the blue line. The green line describes the behavior of the online analysis, if the first pedestal value of a pixel gain channel of the Heidelberg calibration is used as the pedestal start value in the online analysis. The combination of not using nodes, as well as using Heidelberg pedestal start values, is plotted in purple. It is obvious, that the corrected LowGain distribution of the online analysis has more outlying events, as well as a higher deviation of the LowGain pedestal values. This can be resolved, if correct pedestal start values are used. If no nodes are simulated, the result looks slightly better, too. The combination of no node splitting and better pedestal start values does not result in a better distribution than just using Heidelberg pedestal start values.*

of the usage of the wrong Hemisphere will be studied. The second step will be the examination of the influence of the different pedestal values, mentioned in Subsection 6.3.1. At last, the change of the Hillas parameter distributions due to a correct calibration will be shown. As mentioned in Section 6.2, the online analysis assumes, that every observed target is located in the Southern Hemisphere. Therefore, the event selection using the shower parameters is changed accordingly, as well as the shower energy reconstruction. If the Crab Nebula is observed, which is located in the Northern Hemisphere, a change in the distribution of the *mean reduced scaled length* and *width* is expected. This is shown in Figure 6.5 for the offline analysis distribution, as well as for two online analysis ones. One of the online analysis distributions uses the right Hemisphere and one does not. It is easy to see, that both online

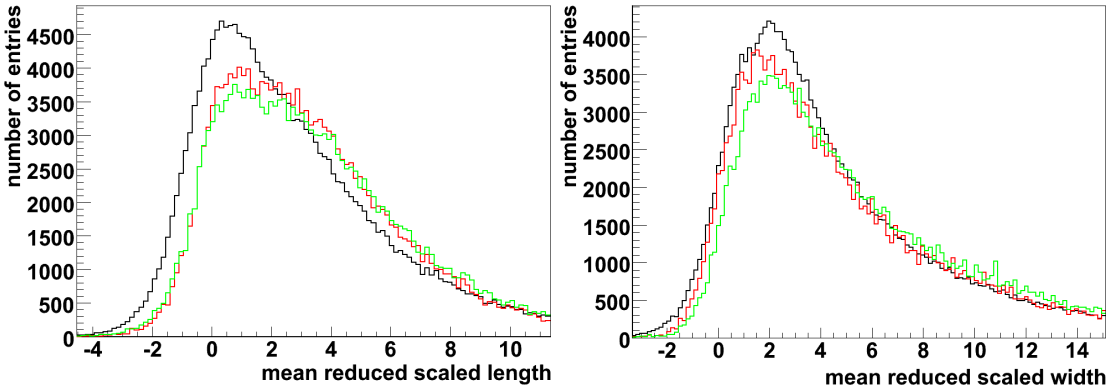

Figure 6.5: *The number of reconstructed events for a Crab Nebula observation run as a function of the mean reduced scaled length and width are plotted in this order. The distribution of an offline analysis is drawn in black, the one obtained using an online calibration is drawn in red. The online calibration reproduces fewer events, as well as broader distributions. If the location of the Crab Nebula is correctly assumed to be on the Northern Hemisphere, the resulting distribution is drawn in green. A slight change in the mean reduced scaled Hillas parameters is visible.*

analysis distributions are shifted to the right. Furthermore, the offline length distribution is thinner.
With comparable pedestal distributions, as shown in Figure 6.4, no significant influence of the different pedestal estimation methods is expected. The confirmation is seen in Figure 6.6. A change in the distributions of the Hillas parameter is not recognizable. However, the influence of the minimal *image amplitude* of 80 p.e. is clearly visible as a sharp cut in the the lower left plot, as well as a reduction in the number of entries in the other plots. The different shape of the *image amplitude* distribution is noteworthy, too. The reason are the standard calibration values, mentioned in Section 6.2, which lead to a lower *image amplitude*.
If the standard calibration values are replaced with the correct ones, the reconstructed *image amplitude* of the shower should match the offline analysis one. This can be seen in Figure 6.7, as well as the result, if no minimal *image amplitude* is required. Moreover, the marginal influence, if broken pixels are excluded, is shown as well. It is obvious, that the *image amplitude* is now properly reconstructed and the number of events of the distributions now match. In addition to that, the use of proper calibration values increases the number of events surviving the minimal *image amplitude* cut, as well as the number of events with high *mean reduced scaled length* and *width* values.

6.3.3 Point sources

To study the influence of the different modifications made to the online analysis in comparison to the offline analysis, 54 observation runs on the Cab Nebula, as the most prominent point-like gamma-ray source in the sky, were used. For an easy, reproducible and more flexible comparison, the online analysis was modified to produce DST-files, instead of the output mentioned before. These resulting online calibrated DST-files contain exactly the same shower information, which would be obtained in real time on site in Namibia. The only difference is, that the splitting of the analysis on the different nodes influences the pedestal values. This had to be emulated. However, it will be shown below that this is negligible. The online calibrated DST-files, as well as the normally calibrated ones, were then processed using HAP

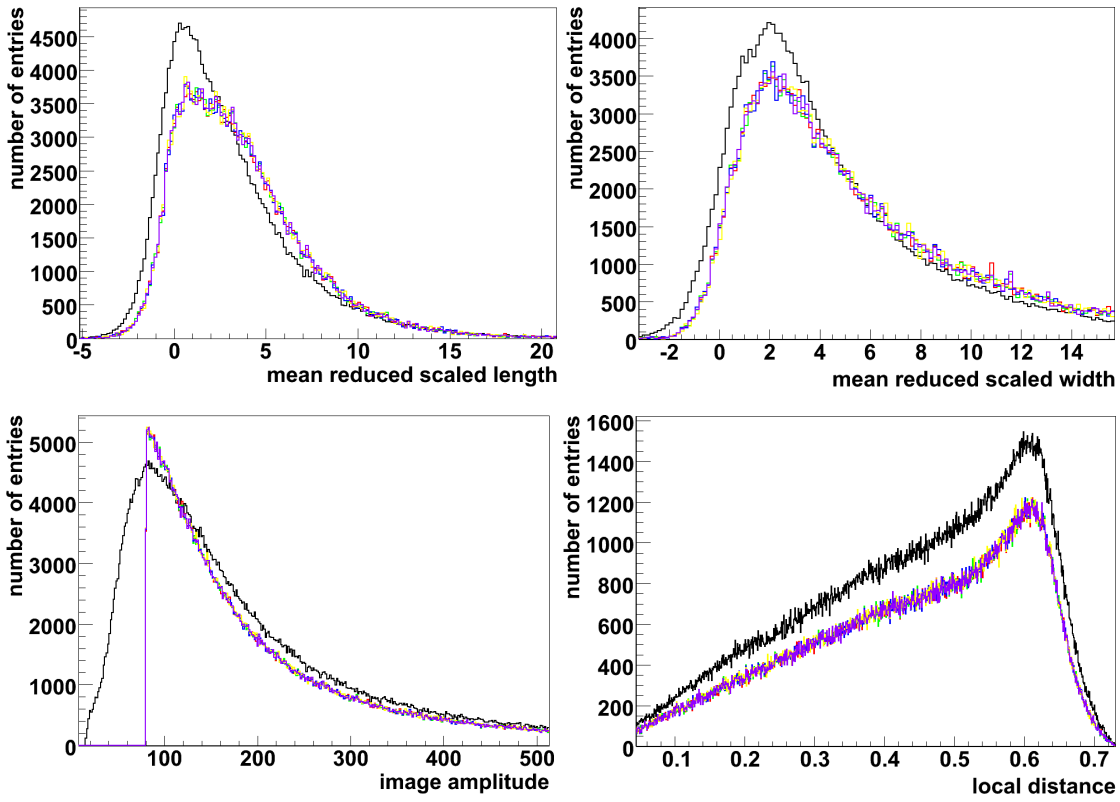

Figure 6.6: *In the upper left and the upper right figure, the distributions of the mean reduced scaled length and width for a Crab Nebula observation run are shown. The number of entries as a function of the image amplitude is plotted on the lower left, as well as the local distance on the lower right. The black line corresponds to the values obtained using the offline calibration. Drawn in red is the distribution of the online analysis Hillas parameters, if the right Hemisphere is used. If additionally no nodes are emulated, the resulting distribution is plotted in green. If Heidelberg pedestal start vales are used, is plotted in blue. The combination of both is purple. If just Heidelberg pedestal values are used, is drawn in yellow. It is clearly visible, that the online analysis distributions don't differ significantly. The sharp cut off, due to the minimal limit of the image amplitude, is seen in the lower left, as well as the lower reconstructed image amplitude due to standard calibration values. The limit is additionally responsible for the lower number of events in the other plots.*

and the WobbleChain. This allowed, for example, the comparison of the extracted spectra of the source, which wouldn't be possible otherwise. To get a first impression of the results of the online analysis, the excess sky map of the 54 observation runs was produced by using the online analysis background maker. This is shown in Figure 6.8 and the point-like shape of the Crab Nebula is obvious.
The different influences on the significance of the detection will be shown in several steps. At first, the influence of the different pedestal estimation methods, mentioned in Subsection 6.3.1 will be examined. After that, the change in the significance of the detection due to other calibration modifications will be presented. Finally, the influence of the event selection will be shown and a fake offline analysis, an online analysis where all modifications were reverted, will be used as a cross check. Additionally, the spectrum and the flux of the source will be compared. As a first step, the change in the significance of the detection of the Crab Nebula was studied, if different pedestal estimation methods were used. As expected, the influence of

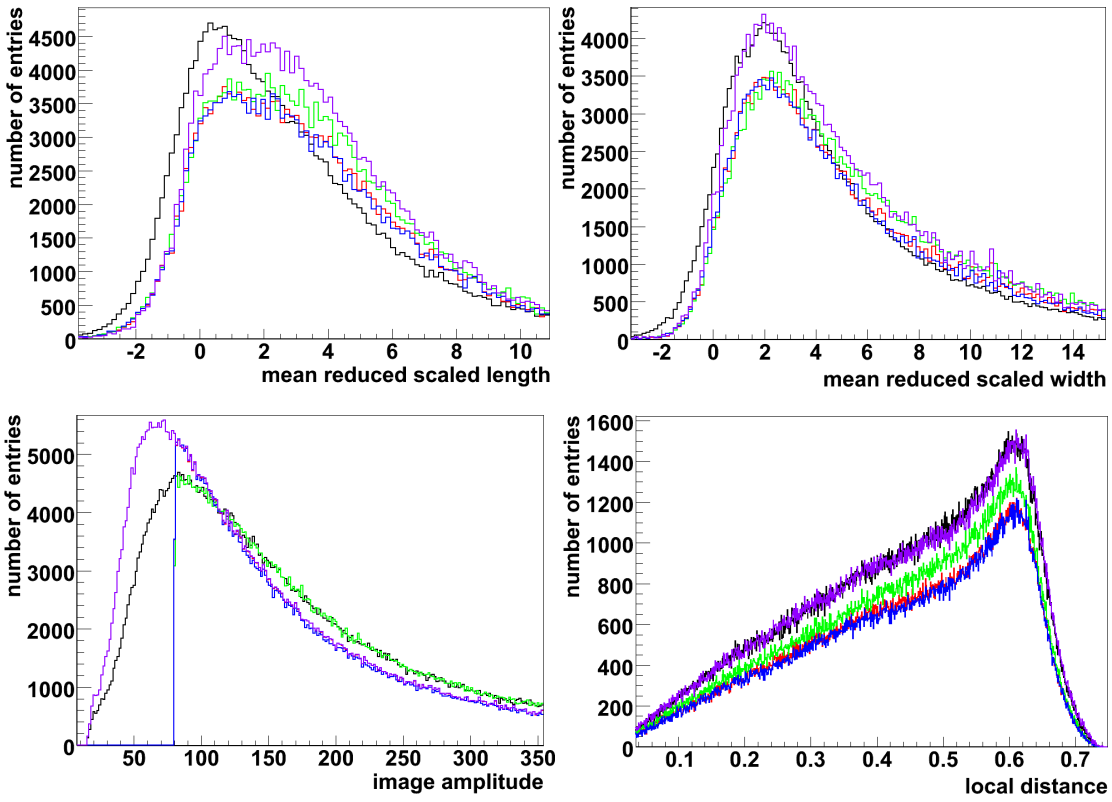

Figure 6.7: *The distribution of the mean reduced scaled length and width are shown in the upper row, as well as the image amplitude and local distance in the lower row for a complete observation run of the Crab Nebula. The black line corresponds to the offline analysis, the other to the online analysis, all using the right Hemisphere for the Crab Nebula and the red line with no further changes. The green line is the result of correct calibration values and the blue one, if broken pixels are excluded. The purple line refers to the missing of the minimal image amplitude cut. The exclusion of broken pixels has no significant influence, but the calibration values result in a correct reconstruction of the image amplitude. The image amplitude cut is responsible for the lower number of events.*

the splitting of the online analysis on different nodes, as well as the usage of better pedestal start values, and the combination of both, doesn't have any visible influence on the significance, as shown in Figure 6.9. If Heidelberg pedestal values are used, an increase in the significance of $\approx 3\,\%$ is seen. This is due to the high weighting factor F and the reduced amount of deviation calculations of the mean pedestal positions. Nonetheless, it is clearly visible that the standard analysis outperforms the online analysis by approximately $16\,\%$. This is true for both the offline analyses, Hap and the WobbleChain.
To further check the different influences of the changes made to the online analysis, the normal calibration values, instead of the default ones, were used, as well as broken pixel were excluded. Furthermore, the correct configuration for the influence of the earth's magnetic field was used. The result of these checks can be seen in Figure 6.10. The correction of the influence of the earth's magnetic field is marginal. The exclusion of broken pixels results in a reduction of the significance. If a pixel appears to be broken, it is disabled for the whole run in the standard analysis. This is done, even if it is broken only for a small part of the run, as seen in Figure 5.14. This could result in more reconstructed events, because pixels

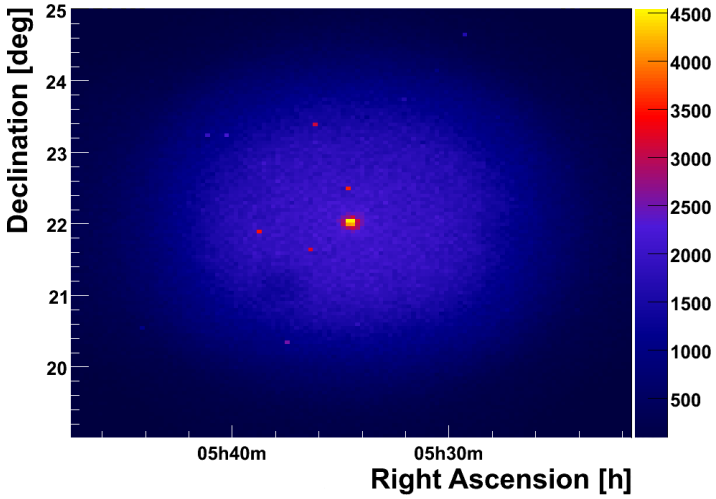

Figure 6.8: *The excess sky map produced by using the online analysis background maker for 54 observation runs of the Crab Nebula is shown. The point-like shape is easy to see.*

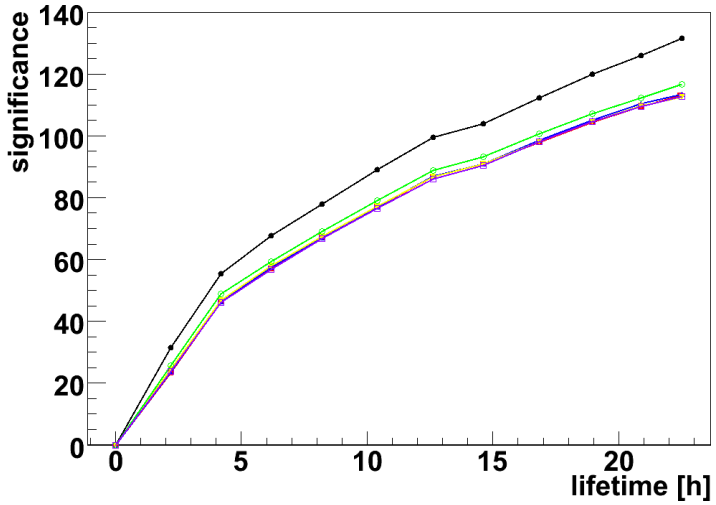

Figure 6.9: *The significance of the detection of the Crab Nebula as a function of the observation time is shown for a set of 54 runs. The black line indicates the use of standard calibrated DST-files with a HAP analysis. The red line corresponds to online calibrated DST-files. If Heidelberg pedestal start values are used in the online analysis, is drawn in blue, if no node splitting is emulated, is in yellow and the combination of both is in purple. The green line is obtained using just Heidelberg pedestal values in the online analysis. No significant influence of the different pedestal values is visible, except for the Heidelberg pedestals. This is because of a too high weighting factor F and a reduced amount of deviation calculations of the mean pedestal position. The standard analysis is* $\approx 16\,\%$ *better than the online analysis.*

are used, which are falsely flagged as broken, thus increasing the significance. The influence of properly calibrated pixel intensities is obvious and expected, because of the change in the Hillas distributions, as seen in Figure 6.7. The change in the flux and the spectrum of the Crab Nebula, due to those alterations, is compatible within the error margins. Another influence on the detection of the Crab Nebula is, that the cuts on the MRSL and the MRSW are optimized for the standard analyses distributions and not for the online analysis ones. This would lead to a reduction of the significance as well.

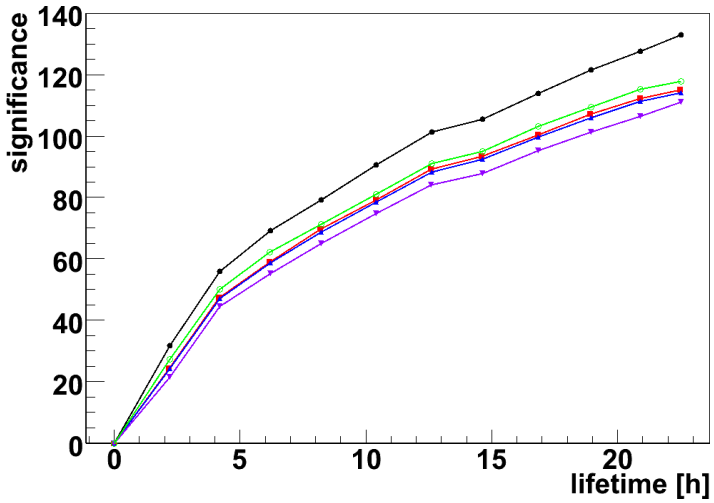

Figure 6.10: *The significance as a function of the lifetime for a set of 54 Crab Nebula observation runs, analyzed using HAP, is plotted. The black line was obtained by using standard calibrated DST-files, the red line with online calibrated ones. The blue line properly corrects for the influence of the earth's magnetic field. The green line uses standard calibration values instead of default values and the purple line excludes broken pixels.*

The highest influence on the significance of the detection of the Crab Nebula is due to cuts on the Hillas parameters, as shown in Figure 6.11. The online analysis uses two cuts on the *mean reduced scaled length* and *width*, which could be identified to be responsible for the difference. It turned out, that the distributions of the mean scaled reduced parameters are different, as seen in Subsection 6.3.2. This results in a different number of events that survive those cuts. A difficulty determining this behavior was the complex interaction of the cuts on the Hillas parameter itself and the *mean reduced scaled* parameters. In detail, an increase in the number of events surviving the cuts could lead to a lower signal to noise ratio and thus to a lower significance. Finally, the changes to the online analysis were reverted to simulate the behavior of the standard DST creation and analysis as a cross check to the results. This fake offline analysis differs only $\approx 1\,\%$ from the standard analysis and thus confirms the result obtained.
At last, the spectra of the online analysis, the fake offline analysis and the standard analysis were compared. Figure 6.12 shows that the flux of the online analysis is smaller than the other two. However, the index of the spectrum is comparable within the error margins. As expected, the flux and the spectrum of the fake offline and the standard analysis match.

6.3.4 Extended sources

Because the online analysis is optimized for the detection of strong point-like sources, the ability to deal with large extended sources will be examined here. To do this 99 observation runs, with the supernova remnant RX J1713.7−3946 as a target, are used. Its large extent of $\approx 1.3°$ [24], should result in an overlap of the off and on regions of the background estimation method of the online analysis. This should reduce the significance of the detection of the source and distort the excess sky map. The standard analysis, which is used to compare the online analysis results to, is a HAP analysis, which is tuned for an extended source. A theta square cut of $0.36\,\mathrm{deg}^2$ is used for that. A comparison of the significance of the detection of

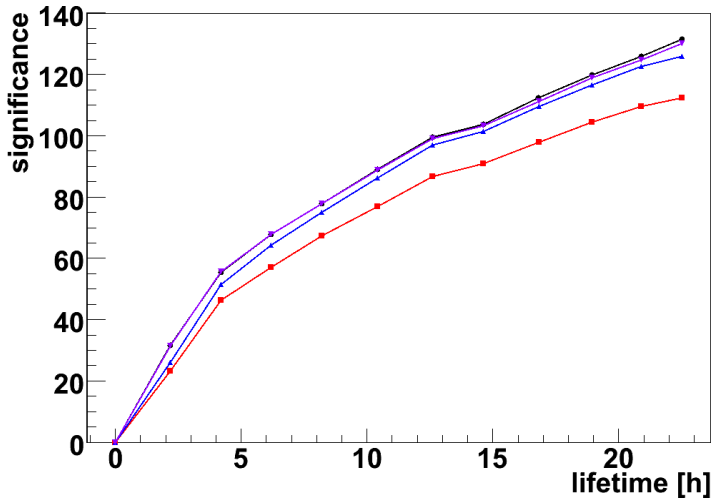

Figure 6.11: *The significance as a function of the lifetime for the Crab Nebula analyzed using HAP. The online analysis is drawn in red, the offline analysis in black. The influence of the cuts on the Hillas parameter (blue line) is clearly visible. The purple line is the result of an online analysis which was modified to emulate offline behavior and matches nicely the offline analysis.*

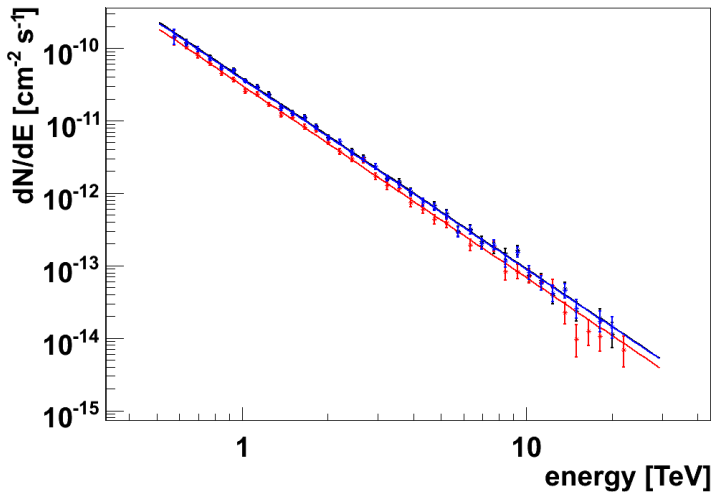

Figure 6.12: *The spectrum of a set of 54 Crab Nebula observation runs analyzed with Hap is shown. The online analysis spectrum (red) has an index of* -2.648 ± 0.02246 *and a flux above* $0.2\ TeV$ *of* $(2.614 \pm 0.07743) \cdot 10^{-10}\ cm^{-2}\ s^{-1}$*. The offline analysis spectrum (black line) has an index of* -2.628 ± 0.02001 *and a flux above* $0.2\ TeV$ *of* $(3.243 \pm 0.08539) \cdot 10^{-10}\ cm^{-2}\ s^{-1}$*. The fake offline analysis spectrum (blue line) has an index of* -2.624 ± 0.0204 *and a flux above* $0.2\ TeV$ *of* $(3.13 \pm 0.0838) \cdot 10^{-10}\ cm^{-2}\ s^{-1}$*. The online analysis has a lower flux than the offline analysis. The index, however, is compatible within the error margins. The fake offline analysis reproduces the result of the offline analysis.*

the source of the online analysis with the HAP analysis, visible in Figure 6.13, confirms the overlap, because the significance of the online analysis is considerably reduced compared to the HAP analysis. Nonetheless, the online analysis would confirm gamma radiation from the direction of the source. If the same background estimation is used as in the HAP analysis, a result similar to the one in Subsection 6.3.3 is obtained. Meaning, that the remaining difference in the significance of the detection is due to the influences mentioned there.
The loss of information due to a wrong background estimation is also visible in the excess

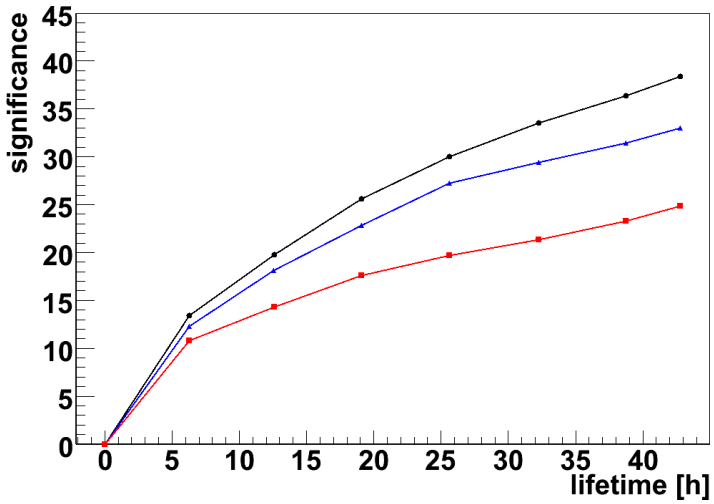

Figure 6.13: *The significance of the detection of RX J1713.7−3946 as a function of the lifetime is plotted for a HAP analysis in black and an unaltered online analysis in red. The blue line corresponds to an online analysis using the same background estimation method as the HAP analysis. The problems of the online analysis dealing with large extended sources are obvious.*

sky map, which is generated by the online analysis. It is filled in a field of view of 3° and can be seen in Figure 6.14. The excess map was smoothed with a Gaussian using a sigma of 0.1. Additionally, the excess sky map of a HAP analysis using hard cuts [14], and smoothed using the same Gaussian, is shown as well. The excess sky map of the online analysis doesn't contain any information about the source

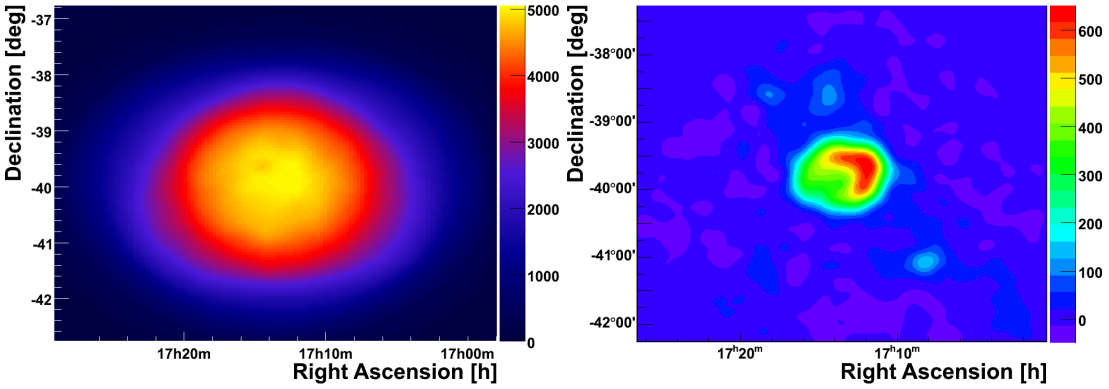

Figure 6.14: *The online analysis excess sky map, smoothed with a Gaussian using a sigma of 0.1, is shown on the left. The excess sky map as a result of a HAP analysis, using hard cuts and smoothed the same way as the online analysis excess sky map, is plotted on the right for the set of 99 observation runs on RX J1713.7−3946. No information about the source can be extracted from the online analysis sky excess map.*

If a proper background estimation would be used by the online analysis, the resulting spectra extracted from the complete on region would be comparable. This can be seen in Figure 6.15. The calculated spectrum of the offline analysis and of the modified online analysis are similar and compatible within the error margins.

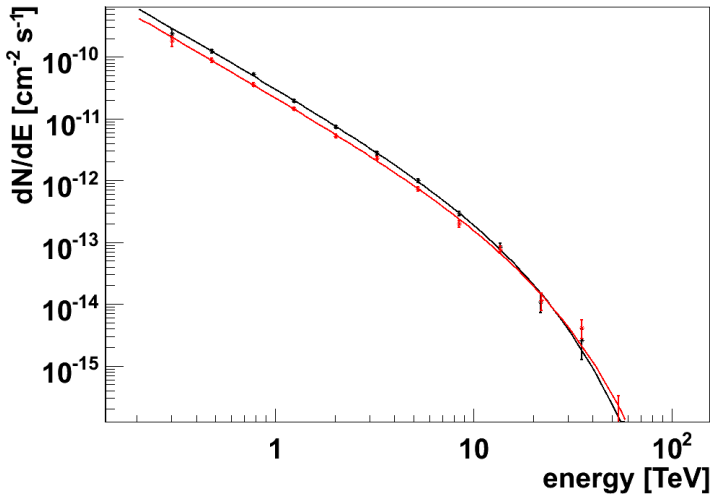

Figure 6.15: *Spectrum generated out of the 99 observation runs with RX J*1713.7−3946 *as a target for the HAP analysis (black line) and the online analysis with a proper background estimation method usable for extended source (red line). The indexes for the spectrum of the offline and online analysis are* -1.838 ± 0.04414 *and* -1.838 ± 0.0516 *with a cut off at* 10.71 ± 1.389 *TeV and* 12.67 ± 2.186 *TeV. The fluxes above above* 0.2 *TeV are* $(1.365\pm0.05684)\cdot10^{-10}$ cm^{-2} s^{-1} *and* $(0.9809\pm0.04796)\cdot10^{-10}$ cm^{-2} s^{-1} *respectively. The results are comparable within their error margins.*

7 Conclusion and Outlook

In the course of this thesis the calibration of the H.E.S.S. cameras was discussed in detail and its importance for the data analysis was shown. The validity of the values for the read out window of the photomultipliers of the H.E.S.S. cameras were checked. Furthermore, the systematic effects of different shower parameters on the read out windows have been examined and proven to be understood and under control. The long term stability of the calibration of the H.E.S.S. cameras was confirmed to be very good and it doesn't suffer from strong fluctuations. The main focus of this thesis was the development of the improved pedestal estimation method, based on a running average calculation, and its verification. A systematic comparison with the two baseline estimation methods, used for data analysis, was done and it was shown, that the improved pedestal estimation method is producing compatible results. This includes pedestals and Hillas parameter distributions, as well as the significance of the detection of a source, its spectrum and its flux. In addition to that, the supremacy of the improved pedestal estimation method was shown for the correction of the baseline oscillations and rapid drifts or jumps of the baseline of pixels. At last, the online analysis, a real time analysis running in parallel with the data taking in Namibia, was presented and its differences from a standard Hillas analysis were shown. Moreover, the different influences on the results of the online analysis were examined for two point-like sources and an extended source. In detail, the influences of the different pedestal estimation method, the default calibration values and the fixed analysis settings on the pedestal and Hillas distributions, as well as the characteristics of a source, i.e. its detection significance, its sky map, its flux and its spectrum, were studied. It was proven, that the online analysis produces compatible results, if a point-like source is observed. However, for an extended source the problems with the background estimation are severe.
In the near future the computer cluster in Namibia will be updated to be ready for the higher data rates of the H.E.S.S. phase II camera. A major overhaul of the online analysis is planned after this, upgrading it to a state of the art Hillas analysis with the option to choose between different background estimation methods and using the improved pedestal estimation method. Additionally, with the necessary changes to the data calibration software, due to the inauguration of the new telescope, the improved pedestal estimation method would be a valid alternative to the currently used pedestal estimation methods.

Bibliography

[1] H.E.S.S. collaboration, F. Acero et al. Detection of Gamma Rays from a Starburst Galaxy. *Science*, 326:1080–1082, 2009.

[2] H.E.S.S. collaboration, F. Aharonian et al. Discovery of very high energy gamma-ray emission from Centaurus A with H.E.S.S. *Astrophys. Journal Lett.*, 695:40–44, 2009.

[3] H.E.S.S. collaboration, F. Acero et al. First detection of VHE gamma-rays from SN 1006 by H.E.S.S. 2010.

[4] T. C. Weekes et al. Observation of TeV gamma rays from the Crab nebula using the atmospheric Cerenkov imaging technique. *The Astrophysical Journal*, 342:379–395, 1989.

[5] S. Wakely, D. Horan. TeVCat Source Catalog. http://tevcat.uchicago.edu, 2010.

[6] H.E.S.S. collaboration, F. Aharonian. et al. The H.E.S.S. Survey of the inner galaxy in very high gamma rays. *The Astrophysical Journal*, 636:777–797, 2006.

[7] R.C.G. Chaves for the H.E.S.S. collaboration. Extending the H.E.S.S. Galactic Plane Survey. *Proc. 31st Int. Cosmic Ray Conference*, 2009.

[8] W. Galbraith and J. V. Jelly. Light Pulses from the Night Sky associated with Cosmic Rays. *Nature*, 171:349–350, 1953.

[9] W. Heitler. *Quantum Theory of Radiation*. Oxford University Press, 1954.

[10] D. Göring. Analysis of the Poisson Structure of H.E.S.S. Sky Maps with Minkowski Functionals. Master's thesis, Friedrich-Alexander-University Erlangen-Nuremberg, 2008.

[11] D. Berge. *The gamma-ray supernova remnant RX J1713.7-3946 with H.E.S.S.* PhD thesis, Ruperto-Carola University of Heidelberg, 2006.

[12] A. M. Hillas. Cherenkov light images of eas produced by primary gamma. *Proc. 19th Int. Cosmic Ray Conference*, 3:445–448, 1985.

[13] J. Brucker. Investigation of H.E.S.S. skymaps by means of Minkowski Functionals. Master's thesis, Friedrich-Alexander-University Erlangen-Nuremberg, 2007.

[14] H.E.S.S. collaboration, F. Aharonian et al. Observations of the Crab Nebula with H.E.S.S. *Astron. Astrophys.*, 457:899–915, 2006.

[15] P. Vincent et al. for the H.E.S.S. collaboration. H.E.S.S. Phase II. *Proc. 29th Int. Cosmic Ray Conference*, 5:163–166, 2005.

[16] J. M. Davies, E. S. Cotton. Design of the quartermaster solar furnace. *Solar Energy*, 1:16–22, 1957.

[17] H.E.S.S. collaboration, F. Acero et al. Localizing the VHE gamma-ray source at the Galactic Centre. *MNRAS*, 402:1877–1882, 2010.

[18] P. Vincent et al. for the H.E.S.S. collaboration. Performance of the H.E.S.S. cameras. *Proc. 28th Int. Cosmic Ray Conference*, 1:2887, 2003.

[19] K. Bernlöhr et al. The optical system of the H.E.S.S. imaging atmospheric Cherenkov telescopes Part I: layout and components of the system. *Astropart. Phys.*, 20:111–128, 2003.

[20] H.E.S.S. collaboration, F. Aharonian et al. Calibration of cameras of the H.E.S.S. detector. *Astropart. Phys.*, 22:109–125, 2004.

[21] H.E.S.S. collaboration, F. Aharonian et al. An exceptional VHE gamma-ray flare of PKS 2155-304. *Astrophys. Journal Lett.*, 664:L71–L74, 2007.

[22] T. Li, Y. Ma. Analysis methods for results in gamma-ray astronomy. *The Astrophysical Journal*, 272:317–324, 1983.

[23] S. Funk. Online Analysis of Gamma-ray Sources with H.E.S.S. Master's thesis, Humboldt-University Berlin, 2005.

[24] D. Berge et al. for the H.E.S.S. collaboration. Primary particle acceleration above 100 TeV in the shell-type Supernova Remnant RX J1713.7–3946 with deep H.E.S.S. observations. *Proc. 30th Int. Cosmic Ray Conference*, 2007.

Danksagung

Zum Schluss möchte ich mich bei all denjenigen bedanken, die mich während der Anfertigung meiner Diplomarbeit unterstützt haben. Insbesondere:

- Der H.E.S.S. Gruppe Erlangen, sowie dem restlichen ECAP, für eine tolle Arbeitsatmosphäre und entspannte Kaffeerunden.
- Prof. Christian Stegmann für seine Fähigkeit einen für das Fachgebiet zu faszinieren, die interessante Aufgabenstellung, die Betreuung, sowie für die morgendlichen Kaffeerunden und seine Bereitschaft meine Fragen zu jeder Zeit zu beantworten.
- Dr. Ira Jung, sowohl für ihre große Hilfsbereitschaft und die Betreuung, als auch für die inspirierenden Diskussionen und die wertvollen Tipps zu der Gestaltung und dem Inhalt dieser Diplomarbeit.
- Sebastian Heinz für sein offenes Ohr für Probleme und seine nützlichen Ratschläge. Außerdem für das Korrekturlesen kurz vor seinem Urlaub.
- Julia Brucker für ihr intensives Korrekturlesen und den umfassenden Tipps zum Layout.
- Meinen Eltern und meinen Geschwistern für ihre Unterstützung.
- Dem *Clubwurst deluxe* für die Freundschaften, die tolle Zeit und die Ablenkung wenn sie nötig war. Insbesondere DeadlusIV für die gemeinsame Zeit in Regensburg, Kosh & NJB2107 für die gemeinsame Zeit in unserer WG in Erlangen, sowie Archy, L3xx, Marksman, Markus und Pink.

Erklärung

Hiermit bestätige ich, dass ich diese Arbeit selbstständig und nur unter Verwendung der angegebenen Hilfsmittel angefertigt habe.

Erlangen, 31. Mai 2010